Universiteit Antwerpen

This item is the archived peer-reviewed author-version of:

Can plasma be formed in catalyst pores? A modeling investigation

Reference:

Zhang Yu-Ru, Van Laer Koen, Neyts Erik, Bogaerts Annemie.- Can plasma be formed in catalyst pores? A modeling investigation

Applied catalysis : B : environmental - ISSN 0926-3373 - 185(2016), p. 56-67

Full text (Publishers DOI): http://dx.doi.org/doi:10.1016/j.apcatb.2015.12.009

uantwerpen.be

Institutional repository IRUA

Can plasma be formed in catalyst pores?

A modeling investigation

Yu-Ru Zhang[a,b], Koen Van Laer[b], Erik C. Neyts[b] and Annemie Bogaerts[b,*]

[a]*Key Laboratory of Materials Modification by Laser, Ion, and Electron Beams (Ministry of Education), School of Physics and Optoelectronic Technology, Dalian University of Technology, Dalian 116024, People's Republic of China*

[b]*Research group PLASMANT, Department of Chemistry, University of Antwerp, Universiteitsplein 1, BE-2610 Wilrijk-Antwerp, Belgium*

Abstract

We investigate microdischarge formation inside catalyst pores by a two-dimensional fluid model for various pore sizes in the μm-range and for various applied voltages. Indeed, this is a poorly understood phenomenon in plasma catalysis. The calculations are performed for a dielectric barrier discharge in helium, at atmospheric pressure. The electron and ion densities, electron temperature, electric field and potential, as well as the electron impact ionization and excitation rate and the densities of excited plasma species, are examined for a better understanding of the characteristics of the plasma inside a pore. The results indicate that the pore size and the applied voltage are critical parameters for the formation of a microdischarge inside a pore. At an applied voltage of 20 kV, our calculations reveal that the ionization mainly takes place inside the pore, and the electron density shows a significant increase near and in the pore for pore sizes larger than 200 μm, whereas the effect of the pore on the total ion density is evident even for 10 μm pores. When the pore size is fixed at 30 μm, the presence of the pore has no significant influence on the plasma properties at an applied voltage of 2 kV. Upon increasing the voltage, the ionization process is enhanced due to the strong electric field and high electron temperature, and the ion density shows a remarkable increase near and in the pore for voltages above 10 kV. These results indicate that the plasma species can be formed inside pores of structured catalysts (in the μm range), and they may interact with the catalyst surface, and affect the plasma catalytic process.

Keywords: plasma catalysis, fluid simulation, microdischarge, pore size, applied voltage

* Corresponding author. Tel.: +32-3-265.23.77; fax: +32-3-265.23.43.

E-mail address: annemie.bogaerts@uantwerpen.be (A. Bogaerts)

1. Introduction

In recent years, there is growing interest for plasma catalysis as an effective technology for environmental protection, like gaseous pollutant removal, hydrocarbon reforming and CO_2 conversion into value-added chemicals [1-6]. Plasma catalysis builds on the integration of a plasma and a catalyst, for an improved performance, i.e., a higher energy efficiency and a better product selectivity [7-16]. This is called the synergistic effect in plasma catalysis. The catalyst can either be placed in the plasma zone, so-called single-stage plasma catalysis, or the plasma and catalyst can be physically separated, so-called two-stage plasma catalysis. In single-stage systems, the plasma interacts directly with the catalyst, and this interaction in turn directly influences the properties of both the plasma and the catalyst. This mutual interaction is causing the possible synergistic effects.

Clearly, the synergistic effect in plasma catalysis is rather complicated. On one hand, the existence of abundant short-lived active species (i.e., ions, radicals, and excited species) in the plasma affects the catalyst properties, such as its morphology or its work function [17-22]. On the other hand, by including a catalyst in the plasma zone, the discharge characteristics will be modified [23-27]. For instance, the presence of a catalyst might significantly enhance the electric field, and the adsorption of pollutants on the catalyst surface may lead to a longer residence time and thus a higher pollutant destruction efficiency. Moreover, some researchers reported the formation of microdischarges inside catalyst pores as another important effect in plasma catalysis, which has a significant influence on the plasma properties [28-33]. Indeed, the strong electric field inside pores leads to different electron energy distributions. This, in turn, gives rise to modified electron impact reaction rates and changes in the plasma chemistry and in the plasma performance for environmental applications.

The existence of short-lived oxidants in the interior of porous catalysts has been experimentally revealed by Holzer et al., for typical pore sizes in the order of 10 nm [28, 29]. They concluded that these short-lived species might be formed inside the pores, if the electric field there was much stronger than in the bulk plasma. In addition, the stabilization of short-lived species by adsorption on the surface during their diffusion from the plasma into pores might be another explanation, as it significantly increases their lifetime and gives rise to the availability of these species for subsequent surface reactions. Furthermore, the same authors investigated the influence of ferroelectric materials on the performance of non-thermal plasmas for the removal of air pollutants [30]. The results indicated that for a constant applied voltage, the energy input in a reactor filled with ferroelectric pellets was 6-10 times higher

than in an empty reactor. This was attributed to the formation of strong microdischarges inside intra- and inter-particle pores (with particle size in the range of 1000 ~ 5000 μm) upon introducing ferroelectric pellets into the plasma zone.

In order to obtain a better insight in the microdischarge properties inside pores, Hensel et al. [31] focused on porous ceramic materials in a direct current (DC) hybrid plasma-catalyst system, in the context of pollutant abatement from car exhaust. They demonstrated that for a pore size of 0.8 μm, the discharge only developed on the dielectric surface (so-called surface discharge). However, for a pore size of 15 μm, a transition in discharge mode was observed above the threshold voltage (i.e., 8.6 kV), and microdischarges inside the ceramic were observed. Subsequently, by using an alternating current (AC) high voltage source, they studied the physical properties of microdischarges for various pore sizes, discharge powers, and gas mixtures [32]. The onset voltage of microdischarge formation was found to decrease with increasing pore size, and a different behavior was seen in oxygen and in nitrogen. Indeed, in oxygen gas, the microdischarge channels mostly concentrated around the outer circumference of the ceramic, while a homogeneous distribution was observed in nitrogen. In a follow-up study, the pore size and the amplitude of the applied voltage were identified as the critical parameters for microdischarge formation [33]. When a porous dielectric layer was present at the electrode, charged species generated by the discharge accumulated on the surface. If the voltage drop across the layer exceeded a critical value, the discharge may leak into the porous ceramic.

The generation of a stable plasma inside catalyst pores is a very important factor for plasma catalysis, as it determines the active surface of the catalyst that is available for the reaction. Therefore, it is of uttermost importance to understand the plasma properties and the mechanisms of microdischarge formation inside pores. However, although some effort has already been put in studying microdischarges inside pores, all of the studies mentioned above are performed experimentally, and the inherent mechanisms behind the formation of microdischarges, as well as their influence on the plasma phase, remain poorly understood. In the present work, we therefore investigate microdischarge formation as a function of pore size and applied voltage, by using a two-dimensional fluid model. The calculations are performed for a helium dielectric barrier discharge (DBD) sustained by an AC source, with the applied voltage varying from 2 kV to 100 kV, which are typical values in DBDs [34, 35]. Although catalyst pore sizes are typically in the microporous (< 2 nm) and mesoporous (2 ~ 50 nm) range, the interparticle meso-macro (μm) pores in structured catalysts are also of crucial

importance in catalysis, e.g., for the pressure drop, and mass and heat transfer of catalysts [30, 36-39]. Besides, for typical DBD plasma conditions (i.e., electron density (n_e) of 10^{17} m^{-3} and electron temperature (T_e) of 3 eV), the Debye length is about 40 μm, which suggests that microdischarges cannot be formed in sub-μm pores. Therefore, pores with sizes in the range of 10 μm ~ 400 μm are considered in this work, for investigating the effect of the pore size on the microdischarge formation.

2. Description of the model

A two-dimensional fluid model is developed within the COMSOL simulation software [40]. In the model, the continuity equations for the electron density and mean electron energy are solved

$$\frac{\partial}{\partial t}\left(n_e\right)+\nabla\cdot\left[-n_e\left(\mu_e\cdot\mathbf{E}\right)-D_e\cdot\nabla n_e\right]=R_e,$$

$$\frac{\partial}{\partial t}\left(n_\varepsilon\right)+\nabla\cdot\left[-n_\varepsilon\left(\mu_\varepsilon\cdot\mathbf{E}\right)-D_\varepsilon\cdot\nabla n_\varepsilon\right]+\mathbf{E}\cdot\left[-n_e\left(\mu_e\cdot\mathbf{E}\right)-D_e\cdot\nabla n_e\right]=R_\varepsilon.$$

Here, n_e and n_ε are the electron density and mean electron energy density; μ_e, D_e, μ_ε and D_ε are the electron mobility, electron diffusivity, energy mobility and energy diffusivity, respectively; R_e and R_ε are the source terms for the electron density and electron energy.

For the heavy species (i.e., ions and neutral species, see below), the following continuity equation is solved

$$\rho\frac{\partial}{\partial t}\left(w_k\right)+\rho\left(\mathbf{u}\cdot\nabla\right)w_k=\nabla\cdot\mathbf{j_k}+R_k.$$

Here, ρ is the density of the mixture; $\mathbf{u}$ is the mass averaged fluid velocity; w_k and R_k are the mass fraction and source term for species k. $\mathbf{j_k}$ represents the flux for species k

$$\mathbf{j_k}=\rho w_k D_k\left(\frac{\nabla w_k}{w_k}+\frac{\nabla M_n}{M_n}\right)-\rho w_k z_k\mu_k\mathbf{E},$$

where D_k, z_k and μ_k are the diffusion coefficient, charge and mobility for species k, and M_n is the mean molar mass of the mixture. Note that for neutral species, the migration term is neglected, i.e., $\mathbf{j_k}=\rho w_k D_k\left(\frac{\nabla w_k}{w_k}+\frac{\nabla M_n}{M_n}\right)$.

The temperature of the other species (so-called heavy particles) is assumed to be 300 K. Transport of electrons is described by the drift-diffusion approximation. The rate coefficients

are adopted from literature for the heavy-particle reactions, while they are obtained from solving the Boltzmann equation for the electrons. The Boltzmann equation also provides the transport coefficients for the electrons. Finally, the electrostatic field is calculated by solving the Poisson equation, based on the space charge density obtained from the charged plasma species densities.

The simulations are performed for a DBD configuration, as shown in Fig. 1(a). The DBD configuration is chosen as it has been mostly used for plasma catalysis applications [22, 23, 28-30, 41]. In this work, both the grounded electrode (made of stainless steel) and the powered electrode (made of nickel) are covered by Al_2O_3 dielectrics ($\varepsilon_r = 9$), with a pore in the bottom layer. The phase of Al_2O_3 (α or γ) is not specified, as this cannot be accounted for in the present model. For this purpose, we would need an atomic-scale model, that can handle the microscopic structure of the material. The pores are always assumed to be vertical, with a fixed aspect ratio of 0.52 (i.e., a 100 μm pore represents a pore with a diameter of 100 μm and a depth of 194 μm). The discharge gap is fixed at 2 mm. We only consider a small section of the discharge, equal to a length of 0.2 mm for pore sizes in the range of 10 μm ~ 100 μm, 0.4 mm for the 200 μm pore, and 0.8 mm for the 400 μm pore, as we want to focus on the plasma behavior near the pore (see Fig. 1). An AC source with a frequency of 25 kHz is applied to the top electrode, and the bottom electrode is grounded. A magnification of the simulated pore structure is shown in Fig. 1(b). There are 7 colored horizontal lines and 1 black vertical line, which indicate the positions where the electric potential will be plotted to illustrate the electrical structure inside the pore, as will be discussed in detail below.

Helium is adopted as the working gas in this model, because it typically gives rise to a homogeneous discharge in a DBD [42], which is easier to describe with a fluid model, and also because its simple chemistry reduces the computational cost. However, it needs to be realized that in reality plasma catalysis is typically performed in reactive gases, such as air or a CO_2/CH_4 mixture, in which streamers are developed and they will affect the plasma catalytic process. Besides, the diffusion coefficients for electrons and charged species in helium are higher than in air, and therefore, the number density of the species transported by diffusion into the catalyst pores will be lower in the case of air. Moreover, the plasma can also be generated along the surface of the catalyst, forming surface streamers. In this case, the parameters of the surface (such as conductivity, the presence of metal nanoparticles and their sizes, roughness, and work function) are important in order to properly describe the behavior of surface streamers. Numerical investigations of plasma catalysis in reactive gases such as air,

focusing on the effect of streamers, as well as on the influence of the catalyst surface properties on the formation of surface streamers, will be performed in our future work.

The following species are taken into account in the model: electrons (e), helium ground state atoms (He), atomic and molecular ions (He^+, He_2^+), metastable dimers (He_2^*) and a combined metastable level (He^*) which includes He(2^1S) and He(2^3S).

The chemical reactions included in the model are presented in Table I, as well as the rate coefficients, and the references where these data are adopted from [43]. The reaction rate coefficients for electron impact elastic collisions, excitation, de-excitation, ionization and Penning ionization (R1-R5) are calculated from energy-dependent collision cross sections using the BOLSIG+ code [44], which is based on solving the spatially-averaged Boltzmann equation. The electron-ion recombination reactions (R7-R14) and the reactions between heavy species (R15-R23) are treated by rate coefficients taken from literature, as a function of electron temperature and/or gas temperature.

The mobilities of the ions are taken from [48], namely 1.0×10^{-3} m^2 V^{-1} s^{-1} for He^+ and 1.6×10^{-3} m^2 V^{-1} s^{-1} for He_2^+, and these values are used in the Einstein relation to calculate the corresponding diffusion coefficients. For the neutral species, the Chapman-Enskog equation is used to calculate the diffusion coefficients, leading to 1.68×10^{-4} m^2 s^{-1} for He and He^* and 1.45×10^{-4} m^2 s^{-1} for He_2^*. Diffusion plays an important role in the transport process. Apart from the gas-phase diffusion, surface diffusion along the catalyst surface might also play a role, but this is not included in the present model. For this purpose, molecular dynamics or Monte Carlo methods need to be applied. This is planned for our future work. On the surface, the atomic and molecular metastable species (i.e. He^* and He_2^*) quench to ground state helium atoms, and the ions (i.e. He^+ and He_2^+) recombine at the surface, and they emit a secondary electron of 5 eV with a probability of 0.05.

A structured mesh (i.e., quadrilateral grid) is used in the bulk region, and it is refined near the top and bottom dielectric plates, i.e., a nonuniform mesh distribution is adopted, and the mesh size near the top and bottom dielectric plates is smaller than in the bulk region. Thus, the mesh size varies in the range between 2 μm (near the top and bottom dielectric plates) and 15 μm (in the bulk region). On the other hand, an unstructured mesh (i.e., triangular grid) is used near and inside the pore, with a resolution of about 0.5 μm for the 10 μm pore, and somewhat larger values for the larger pore sizes (i.e., 1 μm for the 50 μm pore and 4 μm for the 400 μm pore). This mesh allows that reactor-scale and surface-scale processes can be

simultaneously resolved, which means that the plasma behavior both in the bulk region and inside the pore can be accurately described with this mesh structure.

Table 1: Helium reaction set applied in the model, with indication how the rate coefficients are calculated, as well as the corresponding references where these data are adopted from. T_e is the electron temperature in eV, T_g is the gas temperature in eV, and T_g' is the gas temperature in K.

No.	Reaction	Rate Coefficient	Reference
R1	$e + He \rightarrow He + e$	From cross-section	45
R2	$e + He \rightarrow He^* + e$	From cross-section	45
R3	$e + He^* \rightarrow He + e$	From cross-section	44
R4	$e + He \rightarrow He^+ + 2e$	From cross-section	45
R5	$e + He^* \rightarrow He^+ + 2e$	From cross-section	45
R6	$e + He_2^* \rightarrow 2He + e$	3.8×10^{-9} cm^3 s^{-1}	46, 47
R7	$2e + He^+ \rightarrow He^* + e$	$6.0 \times 10^{-20} (T_e/T_g)^{-4.4}$ cm^6 s^{-1}	47
R8	$2e + He_2^+ \rightarrow He^* + He + e$	$4.0 \times 10^{-20} (T_e/T_g)^{-1}$ cm^6 s^{-1}	47
R9	$e + He_2^+ + He \rightarrow He^* + 2He$	$5.0 \times 10^{-27} (T_e/T_g)^{-1}$ cm^6 s^{-1}	47
R10	$2e + He_2^+ \rightarrow He_2^* + e$	$4.0 \times 10^{-20} (T_e/T_g)^{-1}$ cm^6 s^{-1}	47
R11	$e + He_2^+ + He \rightarrow He_2^* + He$	$5.0 \times 10^{-27} (T_e/T_g)^{-1}$ cm^6 s^{-1}	47
R12	$e + He_2^* \rightarrow He_2^+ + 2e$	$9.75 \times 10^{-10} T_e^{0.71} e^{-3.4/Te}$ cm^3 s^{-1}	47
R13	$e + He^+ + He \rightarrow He^* + He$	$1.0 \times 10^{-26} (T_e/T_g)^{-2}$ cm^6 s^{-1}	47
R14	$e + He_2^+ \rightarrow He_2^*$	$5.0 \times 10^{-9} (T_e/T_g)^{-1}$ cm^3 s^{-1}	47
R15	$He^* + He^* \rightarrow He_2^+ + e$	$2.03 \times 10^{-9} (T_g/0.025)^{0.5}$ cm^3 s^{-1}	47
R16	$He^* + He^* \rightarrow He^+ + He + e$	$8.7 \times 10^{-10} (T_g/0.025)^{0.5}$ cm^3 s^{-1}	47
R17	$He^+ + 2He \rightarrow He_2^+ + He$	$1.4 \times 10^{-31} (T_g/0.025)^{-0.6}$ cm^6 s^{-1}	47
R18	$He^* + 2He \rightarrow He_2^* + He$	$8.1 \times 10^{-36} T_g' e^{-650/Tg'}$ cm^6 s^{-1}	47
R19	$He_2^* + He^* \rightarrow He^+ + 2He + e$	$2.03 \times 10^{-9} (T_g/0.025)^{0.5}$ cm^3 s^{-1}	47

R20	$He_2^* + He^* \rightarrow He_2^+ + He + e$	$8.7 \times 10^{-10} (T_g/0.025)^{0.5}$ cm^3 s^{-1}	47
R21	$He_2^* + He_2^* \rightarrow He^+ + 3He + e$	$2.03 \times 10^{-9} (T_g/0.025)^{0.5}$ cm^3 s^{-1}	47
R22	$He_2^* + He_2^* \rightarrow He_2^+ + 2He + e$	$8.7 \times 10^{-10} (T_g/0.025)^{0.5}$ cm^3 s^{-1}	47
R23	$He_2^* + He \rightarrow 3He$	4.9×10^{-22} cm^3 s^{-1}	46

3. Results and discussion

In this paper, the microdischarge properties inside a catalyst pore are investigated for various pore sizes and applied voltages, by examining the spatial distributions of the plasma density, electron temperature, electric field, electron impact ionization rate and electric potential. However, before studying the effect of pore size and voltage, we will first illustrate the calculation results for a fixed pore size (i.e., diameter of 100 μm and depth of 194 μm) and voltage (i.e., amplitude of 20 kV), in order to obtain a general understanding of the microdischarge behavior. .

3.1 Microdischarge properties inside the pore

The calculated time-averaged electron density and total ion density distributions are shown in Fig. 2. In order to visualize more clearly the variation of the plasma density inside the pore, the values are plotted on a log scale. The electron density is found to be uniform throughout the bulk region, with a value around 10^{17} m^{-3}, and it decreases by about 3 orders of magnitude in the sheaths in front of the top and bottom dielectric plates, as well as inside the pore (cf. Fig. 2(a)). The total ion density is equal to the electron density in the bulk plasma, but in the sheaths, the ion density does not show a rapid drop, leading to a positive space charge. Moreover, inside the pore, the total ion density increases even by a factor 7(cf. Fig. 2(b)).

The spatial distributions of the electron temperature and electric field, averaged over time during one cycle, are presented in Fig. 3. The electron temperature (Fig. 3(a)) reaches its minimum in the center. This is because on one hand, the electric field is lower here (i.e., in the order of 10^4 – 10^5 V/m, see Fig. 3(b)), which limits the electron heating. On the other hand, the electrons lose more energy during the frequent collisions in the bulk region. The electron temperature increases in the sheath near the top dielectric plate, and especially inside the pore. This can be explained by the strong electric field, as is clear from Fig. 3(b). Indeed, the electric field inside the pore is significantly enhanced relative to the sheath area, amounting to a value of 1×10^6 V/m, which is about 2.5 times higher than the field strength in the sheath in

front of the top dielectric plate. This enhanced electric field is responsible for the high electron temperature in the pore, up to 6.3 eV. Accordingly, this high electron temperature results in an enhanced ionization (as will be discussed below), which gives rise to the high ion density, reaching a maximum value of about 8.4×10^{17} m^{-3}, as shown in Fig. 2(b) above.

Note that the electric field plotted in Fig. 3(b) is calculated as $\sqrt{E_z^2 + E_r^2}$, where E_z and E_r are the axial and radial electric field, respectively. For this reason, the plotted electric field is always positive. The axial electric field is much stronger than the radial electric field, as can also be deduced from Fig. 6 below. Moreover, during the first half cycle, the axial electric field is strongly negative inside the pore, while during the next half cycle, the situation is opposite, but because the electric field is then much lower, averaged over one cycle, the electric field inside the pore is negative, thus accelerating the ions towards the bottom of the pore and pushing the electrons back into the bulk plasma. This explains the very low electron density, as shown in Fig. 2(a) above.

Fig. 2 indicated that both electrons and ions exist inside the pore. The same is true for the other plasma species, i.e., He^* and He_2^*. The He^* density (Fig. 4(a)) shows a minimum in the bulk region, and it increases by about 4 orders of magnitude in the sheath in front of the top dielectric plate, as well as inside the pore. Moreover, also the He_2^* density is higher inside the pore than in the bulk region, i.e., with maximum value around 7×10^{17} m^{-3}, as is clear from Fig. 4(b).

Bhoj and Kushner have also computationally investigated whether plasma species were able to penetrate into the surface features of a rough polymer surface for a corona discharge in humid air [49]. Although this was not a catalyst surface, the study is partially relevant for our work. Their results indicated that the electrons and ions were able to penetrate only to a limited extent, for pore sizes of about 1 μm, which were comparable to the Debye length. To validate our model, we have applied it to similar conditions as in [49], and we obtained very similar results. This illustrates that the pore size is very important to determine whether plasma species can penetrate, or exist, inside pores.

The availability of plasma species inside the pore is of significant importance for the plasma catalytic process, as their interaction with the surface might affect the morphology and work function of the catalyst, and accordingly influence the catalyst performance in practical applications. Moreover, if the plasma species can exist inside the pores, it will increase the active surface of the catalyst that can participate in the reactions. Holzer et al. [28] suggested that in order to form short-lived species inside the pore (i.e., as a result of a microdischarge),

the local electric field in the pore must be higher than in the bulk gas phase. This is indeed what we clearly observe in Fig. 3(b) above.

In order to elucidate the mechanisms giving rise to the plasma enhancement inside catalyst pores, it is crucial to distinguish whether the plasma species are generated inside the pore, or whether they enter the pore due to diffusion and migration from the bulk and sheath area. To clarify the formation of the species, the electron impact ionization rate is plotted in Fig. 5. Based on the electron impact ionization cross section (in the order of 10^{-21} m^2) and the He atom number density (about 2.4×10^{25} m^{-3} at atmospheric pressure), the mean free path for ionization is about 42 μm, which is smaller than the pore size. Considering the high electron temperature inside the pore (see Fig. 3(a)), the ionization rate reaches its maximum inside the pore, and the value is even one order of magnitude higher than in the sheath near the top dielectric plate. This gives rise to the high ion density inside the pore, as shown in Fig. 2(b). Although the strong electric field also accelerates the ions inside the pore, our calculations reveal that the contribution of migration is one order of magnitude lower than the direct ionization inside the pore. The electron impact ionization rate profile can be considered as evidence for microdischarge formation inside the pore. The electron impact excitation rate exhibits a similar distribution (not shown here), and this is responsible for the high He^* density inside the pore (see Fig. 4(a) above).

For a better understanding of the electrical structure inside the pore, the electric potential distribution in the bottom half of the reactor (i.e., $y \in [-0.5, 1]$ mm) is illustrated in Fig. 6(a). The contour lines help us to clearly see the potential variation. Again, the plotted potential distribution is time-averaged over one cycle. The potential in the bulk region is quite uniform and in the order of 130 V, and it drops only slightly to about 100 V near the bottom dielectric. Inside the pore, however, the potential drops significantly to about -12 V at the bottom. This strong gradient is clear from the high density of the contour lines. Moreover, whereas the contour lines are flat in the reactor center, they curve near the bottom dielectric, especially inside the pore, which indicates the influence of the pore on the discharge properties.

The curved contour lines inside the pore indicate that there is also a potential drop in the horizontal direction, albeit quite small. This is because the electrical structure inside the pore is affected by the strong electric field in the vertical direction, pushing the electrons generated inside the pore back to the bulk region, and thus leaving a positive space charge inside the pore (see difference in electron and total positive ion densities, plotted in Fig. 2 above).

To better visualize this potential drop near the side walls, the potential distributions along the horizontal direction at 7 different positions indicated in Fig. 1(b) are plotted in Fig. 6(b). A black dashed line, indicating the pore, is drawn to help distinguish the potential inside and outside the pore. At the position near the top of the pore, i.e., position 1, the potential distribution in the dielectric is almost constant, which means that the plasma has no significant influence on it. Moreover, the potential inside the pore shows a maximum at the center. The potential drop from the center of the pore to the edge is about 7 V, which might correspond to a small sheath as a result of the positive space charge (cf. above). The potential distributions at the other vertical positions (positions 2-6) are quite similar, i.e., nearly constant inside the dielectric and with a parabolic profile inside the pore. The potential drop from the center to the edge of the pore is always around 7 V. At the position near the bottom of the pore, i.e., position 7, the potential inside the pore exhibits a somewhat less parabolic profile, with a drop of only 3.4 V, and the potential inside the dielectric clearly increases from the pore wall to the bulk of the dielectric. Although our computational region is limited, we expect that the potential in the dielectric far away from the pore should be constant, and it decreases to lower values at the edge of the pore.

Finally, the potential distribution along the vertical direction (see black vertical line in Fig. 1(b)) behaves as expected in a DBD, as shown in Fig. 6(c). The maximum of the potential takes place in the bulk region, as was clear from Fig. 6(a), and it drops rapidly in the sheath near the top dielectric plate, as well as in the pore, from 100 V at the top of the pore to -12 V near the bottom. This explains the strong electric field inside the pore, as illustrated in Fig. 3(b).

3.2 Different behavior for different pore sizes

The pore size was experimentally proven to have a significant influence on the formation of a microdischarge inside the pore [31-33]. In order to gain a better understanding of the microdischarge behavior, we investigated the electron and ion density, electron temperature, electric field, ionization rate and potential distributions for various pore sizes, with the applied voltage fixed at 20 kV. Note that the pore size mentioned here refers to the diameter of the pore. As mentioned above, the aspect ratio is kept constant (i.e., 0.52), so the pore depth increases proportionally with the pore diameter.

Fig. 7 shows the electron density and the total ion density distributions along the vertical centerline from the bottom of the pore (negative y-values) to the top dielectric plate (y = 2 mm) for various pore sizes. The bottom dielectric plate starts at y = 0 mm. When there is no

pore in the bottom dielectric plate, the electron density exhibits a flat distribution in the bulk region (see black solid curve). The maximum appears at the center between the two dielectric plates, and it drops clearly towards the walls, and even more than three orders of magnitude in the sheaths (not visible in this figure). When there is a small pore in the bottom dielectric plate (i.e., with pore size equal to or smaller than 50 μm), the pore does not significantly affect the electron density distribution in the bulk region and in the sheath in front of the top dielectric plate, but the density is slightly enhanced near the bottom dielectric plate, indicating that this small pore still influences the electron density to some extent, through the enhanced ionization process due to the high electron temperature (see below). However, inside the pore, the electron density decreases to low values.

When the pore size is above 50 μm, the electron density profiles become strikingly different. The electron density near and in the pore first increases, and then it drops to low values at the bottom of the pore, resulting in an asymmetric distribution of the electron density along the vertical direction, as was also clear from Fig. 2(a) above. Moreover, the increasing trend becomes more obvious at 400 μm, which indicates the enhanced plasma generation inside the pore (see below).

The different effects of the pore size on the ion density distributions are apparent from Fig. 7(b). The ion density also exhibits a flat distribution in the bulk region, but with higher absolute values in the sheath, due to the enhanced ionization caused by the higher electron temperature (see below). Besides, the ion density increases near and in the pore, which is even obvious when the pore size is only 10 μm. As the pore size becomes larger, this increasing trend becomes more pronounced. For instance, the maximum in the ion density in the 400 μm pore is about 1.2×10^{18} m^{-3}, which is 6 times higher than in the case without pore. This is clear evidence for the enhancement of the discharge.

The distributions of the electron temperature, electric field and electron impact ionization rate along the vertical centerline calculated for various pore sizes are depicted in Fig. 8. In the case without pore, the electron temperature (Fig. 8(a)) exhibits two similar peaks in the sheaths, due to the strong electric field in this region (Fig. 8(b)), and this also gives rise to the high ionization rate (Fig. 8(c)) and ion density (Fig. 7(b)). When there is a 10 μm pore in the dielectric plate, the electron temperature inside the pore shows a remarkable increase, and so does the ionization rate. As the pore size becomes larger, the maximum in the electron temperature decreases significantly, but the absolute value is still much higher than in the case without pore (i.e., 4 eV for the case without pore, and 5.2 eV for the case with a 400 μm pore).

This can be understood by examining the evolution of the electric field with pore size in Fig. 8(b). When there is no pore in the dielectric plate, the electric field is uniform in the bulk region, and it becomes one order of magnitude higher in the sheath, as expected. When a 10 μm pore is present, the electric field in the bulk region and in the sheath near the top dielectric shows a similar behavior, whereas the absolute value inside the pore is about 12 times higher, and this is responsible for the higher electron temperature shown in Fig. 8(a). As the pore size increases, the electric field still exhibits an asymmetric distribution, but the maximum inside the pore decreases, which can be understood by examining the potential distribution below.

However, the evolution of the ionization rate with pore size is different, as is clear from Fig. 8(c). The ionization rate inside the pore first increases when the pore size rises from 10 μm to 20 μm, and then it decreases, with a minimum appearing at a pore size of 100 μm. For still larger pore sizes, the ionization rate increases again, and the value in the 400 μm pore is higher than those obtained at the smaller pore sizes. This is because on one hand, the electron temperature inside the pore decreases with increasing pore size, leading to a lower ionization rate coefficient. On the other hand, the electron density inside the pore is enhanced for larger pore sizes, so there are more electrons available to cause ionization inside the pore. Moreover, although the ionization rate in the small pores (i.e., with pore size equal to or below 30 μm) is higher than in the larger pores (i.e., 50 μm and 100 μm), the ion density increases monotonously with pore size (cf. Fig. 7(b)). This is because on one hand, the effective region for ionization is limited in the small pores, and this accordingly limits the enhancement of the total ion density. On the other hand, more ions are lost at the walls due to the stronger electric field in the small pores, as shown in Fig. 8(b).

Fig. 9 shows the potential distributions near the bottom dielectric plate, obtained for different pore sizes, i.e., 10 μm, 50 μm, and 400 μm. The results obtained for the other pore sizes are not illustrated, but they are similar to those for the 50 μm pore (Fig. 9(b)), and they gradually evolve into the distribution shown for the 400 μm pore (Fig. 9(c)). Only the potential distribution for the 10 μm pore (Fig. 9(a)) is strikingly different from those observed at the larger pore sizes. This clearly indicates that this pore size affects the discharge properties in a different way. Indeed, in this case, the minima of the potential, i.e., the most negative values (around -20 V), appear on the sidewalls, and the maximum (around 40 V) is found at the bottom of the pore. This is because the positive ions are accelerated downwards due to the electric field in the sheath, and they accumulate at the bottom of the pore, resulting in a higher potential there. The same effect also occurs for the larger pore sizes, but in those

cases, more electrons are generated (cf. Fig. 7(a)) and they can neutralize the positive charge accumulated at the bottom of the pore, leading finally to a negative potential (as will be discussed below). In case of the 10 μm pore, the positive potential at the bottom of the pore consequently induces an electric field directed to the top of the pore, which accelerates the electrons downwards, and therefore a large number of electrons accumulate in the region between y = -0.006 mm and y = -0.009 mm, where the influence of the electric field induced at the bottom (directed upwards) counteracts with that generated in the sheath near the bottom dielectric (directed downwards). As the sidewalls are very steep, the positive ions can hardly reach the walls, while the electron flux is more isotropic, so negative charge accumulation takes place on the side walls due to the isotropic movement of the electrons, which gives rise to this negative potential. Moreover, the rapid increase of the potential from -20 V to 40 V over a short distance at the bottom of the pore leads to a strong electric field there, which was also obvious from Fig. 8(b)).

When the pore size increases to 50 μm, the plasma potential decreases monotonously from the top of the pore to the bottom, and the potential also varies slightly in the horizontal direction, with slightly higher values in the center of the pore than at the edge (similar to what was illustrated in Fig. 6(b) above). This indicates that the electrical structure inside the pore becomes different, and microdischarges might form. The generation of microdischarges inside larger pores has also been observed by Hensel et al., in experiments performed in dry air [31]. Their results revealed that at a fixed DC voltage (9.8 kV), the discharge developed on the dielectric surface when using a ceramic with pores of 0.8 μm, whereas microdischarges were generated inside the ceramic with 15 μm and 90 μm pores.

When the pore size is 400 μm (see Fig. 9(c)), a more pronounced sheath is observed, both at the sidewalls and near the bottom. Indeed, the potential is rather constant in the upper part of the pore, but it drops significantly along the vertical direction near the bottom of the pore, as well as in the horizontal direction near the sidewalls. This indicates the stronger microdischarge inside the 400 μm pore, which accordingly explains the enhanced plasma generation inside the pore, as is clear from the electron and total positive ion density distributions in Fig. 7. This is consistent with what we can expect from the theoretical Debye length at the conditions under study (i.e., an electron temperature and density of 5.2 eV and 4.5×10^{17} m^{-3} yield a Debye length of 25 μm).

3.3 Different behavior for different voltages

In order to investigate the influence of the applied voltage on the microdischarge behavior inside the pore, the pore size is now fixed at 30 μm, and the applied voltage is varied in the range of 2 kV ~ 100 kV.

The evolution of the electron density and total ion density as a function of applied voltage is presented in Fig. 10(a) and 10(b), respectively. At the voltage of 2 kV, the electron density exhibits two maxima at about y = 0.5 mm and 1.5 mm, and decreases to low values in the center and in the sheaths near the top and bottom dielectric plates. Especially inside the pore, the absolute value is about 4 orders of magnitude lower (not visible in this figure). These two maxima are explained by the high electron impact ionization rate in the sheaths near the top and bottom dielectric plate. As the voltage increases to 5 kV, the electron density distribution in the bulk region becomes flat, and the same behavior is observed up to a voltage of 20 kV, expect for the absolute value, which increases monotonically with voltage. However, as the voltage rises further, especially up to 100 kV, the electron density is enhanced near the pore, and also slightly inside the pore, which is caused by the enhanced ionization under this condition (see below).

The influence of the voltage on the total ion density is presented in Fig. 10(b). When the voltage is low, i.e., 2 kV, the ion density exhibits a similar distribution as the electron density in the bulk region, and it drops to low values in the sheath, and especially inside the pore. Under this condition, no discharge enhancement due to the pore is observed. Upon rising voltage, the ion density increases due to the enhanced ionization, and the ion density distribution becomes asymmetric, which is especially obvious for voltages above 10 kV. Indeed, the ion density near and in the pore increases faster than at the center, due to the strong electric field, as will be discussed below. At a voltage of 100 kV, the maximum of the ion density inside the pore is 3.5×10^{18} m^{-3}, which is about one order of magnitude higher than the value in the center. This indicates that the discharge behavior becomes strikingly different at higher voltages, and the generation of plasma species inside the pore is significantly enhanced. Hensel et al. also reported, for a fixed pore size of 80 μm, that the intensity of the light emission increased with discharge power [32].

Fig. 11(a) shows the electron temperature distributions along the vertical centerline for different voltages. It is clear that even at low voltage, i.e., 2 kV, the spatial distribution of the electron temperature is asymmetric, and the maximum inside the pore is 5.6 eV, which is about one order of magnitude higher than in the sheath near the top dielectric. This indicates the significant influence of the pore on the plasma characteristics, due to the strong electric

field, as shown in Fig. 11(b). As the voltage increases, the electrons gain more energy, resulting in a higher electron temperature throughout the discharge region, especially in the sheath near the top dielectric plate and inside the pore. This high electron temperature leads to more ionization. Indeed, the ionization mainly takes place in the sheath and inside the pore, and it is significantly enhanced at higher voltages (i.e., maximum of about 1.8×10^{26} $m^{-3}s^{-1}$ at 100 kV, see Fig. 11(c)), which also explains the high electron density and ion density inside the pore, as shown in Fig. 10.

The evolution of the electric field with voltage, as illustrated in Fig. 11(b), is similar to that of the electron temperature. Indeed, the electric field increases with voltage, and the values inside the pore are several times higher than in the sheath near the top dielectric plate. Moreover, the electric field increases rapidly to its maximum over a short distance inside the pore, whereas the increasing trend near the top dielectric is much slower. The stronger electric field and the faster rise inside the pore significantly affect the discharge behavior, as is obvious from the higher electron temperature and the enhanced ionization and plasma density, and this influence becomes more significant at higher voltages.

However, although the enhancement of the electric field inside the pore is prominent already at 2 kV, the discharge behavior is somewhat different from that obtained at higher voltages, as appears from the potential distribution, shown in Fig. 12(a). It is clear that the contour lines of the potential are straight in the region far away from the pore, which indicates that the discharge behavior is not affected here. The potential decreases from 70 V to 34 V at the surface of the bottom dielectric (or top of the pore). Inside the pore, the potential drops further to a minimum of 10 V at a depth of about 0.03-0.05 mm, but it rises again to slightly higher values (i.e., 18 V) at the bottom of the pore. This is because of the positive charge accumulation. Indeed, the ionization inside the pore is not strong enough due to the moderate electron temperature (i.e., 5.6 eV), and thus there are not enough electrons to neutralize this positive charge accumulation, creating a higher potential, which is similar to the behavior illustrated in Fig. 9(a) above.

When the voltage increases to 20 kV, as shown in Fig. 12(b), the potential drop in the sheath in front of the bottom dielectric becomes larger due to the higher applied voltage. The contour lines curve even at a distance of 0.1 mm above the pore, which indicates the influence of the pore on the bulk discharge behavior. Inside the pore, the potential decreases monotonically from the top to the bottom, and the potential distribution along the horizontal direction has a slightly parabolic shape, with the maximum values in the center.

At a voltage of 100 kV, the influence of the pore on the discharge becomes more evident, as illustrated in Fig. 12(c). Indeed, the contour lines in the bulk plasma curve more strongly. Inside the pore, the potential distribution is similar to that observed at 20 kV, except that the potential drop along the vertical direction is larger, and this is responsible for the stronger electric field (see Fig. 11(b)) and the higher ionization rate (see Fig. 11(c)). It is therefore clear that besides the pore size, also the applied voltage plays an important role in the behavior of the microdischarge, and it affects the discharge characteristics prominently.

4. Conclusions

In this work, the microdischarge behavior inside a pore of a catalyst surface is investigated by a two-dimensional fluid model in a helium dielectric barrier discharge. First, the microdischarge behavior is investigated in detail for a fixed pore size (100 μm) and applied voltage (20 kV). The results indicate that the total ion density remarkably increases inside the pore, reaching a value which is a factor 7 higher than in the center of the discharge. Moreover, the electron density shows a slight increase near the pore. This is attributed to the strong electric field inside the pore, which in turn also gives rise to a much higher electron temperature. As a result, the electron impact ionization is also greatly enhanced inside the pore, giving rise to the formation of the ions and electrons. The same applies to electron impact excitation, and the formation of excited plasma species. So we may conclude that the plasma species are generated inside the pore, although the ions might also migrate into the pore due to the strong electric field. The electron density inside the pore is lower than the total positive ion density, because the strong electric field inside the pore pushes the electrons back to the bulk region, and also because the electrons are lost at the walls.

The discharge properties are also investigated for various pore sizes and applied voltages, and the results indicate that these two parameters have a critical influence on the behavior of the microdischarge inside the pore. When the applied voltage is fixed at 20 kV, the electron density in the case without pore exhibits a flat distribution in the bulk region. When a pore is present, the electron density shows a significant increase near and in the pore, especially when the pore size is larger than 200 μm, whereas the effect on the total ion density is evident already for a 10 μm pore. This is because the ionization inside the pore is significantly enhanced due to the high electron temperature, and this leads to the enhanced generation of plasma species inside the pore. Moreover, the pore size affects the electric potential in a different way. Inside a 10 μm pore, the maximum of the potential appears at the bottom of the pore, whereas the potential decreases monotonously from the top of the pore to the bottom

when the pore size is above 20 μm. For a 400 μm pore (which may occur in structured catalysts), the potential drop in both the vertical and the horizontal direction becomes more pronounced, implying the presence of a clear sheath near the bottom of the pore and the side walls, which is a strong evidence for the presence of a microdischarge inside the pore, and this is also consistent with what we can expect from the theoretical Debye length.

Finally, the microdischarge behavior inside the pore is investigated for various applied voltages, with the pore size fixed at 30 μm. When the voltage is low, i.e., 2 kV, the pore has no significant influence on the plasma properties. As the voltage increases, the electric field inside the pore becomes stronger, which gives rise to a higher electron temperature, and thus to a higher ionization rate. The electron density near and in the pore increases at 50 kV, and the increasing trend becomes prominent at 100 kV, whereas the influence on the ion density becomes evident already for voltages above10 kV.

In conclusion, our model predicts that plasma species can be formed inside the pores of structured catalysts, with pore sizes above 10 μm. Indeed, the ionization mainly takes place inside the pore, due to the strong electric field and high electron temperature. The ionization is more pronounced at larger pore sizes and higher applied voltages, leading to a high plasma density near and in the pore, which is also observed by Hensel et al. [31, 32]. If the pore size is 10 μm or lower, no significant ionization takes place inside the pore. However, the plasma species might still be able to penetrate into the pore due to diffusion and migration, and then interact with the catalyst surface [16]. This will be investigated in further work.

The results obtained in this work are of crucial importance for the catalytic performance, as the presence of plasma species inside catalyst pores might affect the physical and chemical properties of the catalyst, and more importantly, it will increase the active surface area of the catalyst that is available for surface reactions, in case of plasma catalysis.

Acknowledgments

This work was supported by the Fund for Scientific Research Flanders (FWO) (Grant No. G.0217.14N), the National Natural Science Foundation of China (Grant No. 11405019), and the China Postdoctoral Science Foundation (Grant No. 2015T80244). The authors are very grateful to V. Meynen for the useful discussions on catalysts. This work was carried out in part using the Turing HPC infrastructure at the CalcUA core facility of the Universiteit Antwerpen, a division of the Flemish Supercomputer Center VSC, funded by the Hercules Foundation, the Flemish Government (department EWI) and the University of Antwerp.

References

[1] E.C. Neyts, K. Ostrikov, M.K. Sunkara, A. Bogaerts, Chem. Rev. 2015, DOI: 10.1021/acs.chemrev.5b00362.

[2] H.L. Chen, H.M. Lee, S.H. Chen, Y. Chao, M.B. Chang, Appl. Catal. B: Environ. 85 (2008) 1.

[3] J. Van Durme, J. Dewulf, C. Leys, H. Van Langenhove, Appl. Catal. B: Environ. 78 (2008) 324.

[4] H.L. Chen, H.M. Lee, S.H. Chen, M.B. Chang, S.J. Yu, S.N. Li, Env. Sci. Technol. 43 (2009) 2216.

[5] J.C. Whitehead, Pure Appl. Chem. 82 (2010) 1329.

[6] E.C. Neyts, A, Bogaerts, J. Phys. D: Appl. Phys. 47 (2014) 224010.

[7] H.K. Song, J.W. Choi, S.H. Yue, H. Lee, B.K. Na, Catal. Today 89 (2004) 27.

[8] T. Nozaki, N. Muto, S. Kado, K. Okazaki, Catal. Today 89 (2004) 57.

[9] J. Van Durme, J. Dewulf, W. Sysmans, C. Leys, H. Van Langenhove, Appl. Catal. B: Environ. 74 (2007) 161.

[10] H. Wang, J. Li, X. Quan, Y. Wu, Appl. Catal. B: Environ. 83 (2008) 72.

[11] X. Tu, H.J. Gallon, M.V. Twigg, P.A. Gorry, J.C. Whitehead, J. Phys. D: Appl. Phys. 44 (2011) 274007.

[12] H.J. Gallon, X. Tu, J.C. Whitehead, Plasma Proc. Polym. 9 (2012) 90.

[13] L.F. Spencer, A.D. Gallimore, Plasma Sources Sci. Technol. 22 (2013) 015019.

[14] H.H. Kim, A. Ogata, S. Futamura, Appl. Catal. B: Environ. 79 (2008) 356.

[15] H.H. Kim, A. Ogata, Eur. Phys. J. Appl. Phys. 55 (2011) 13806.

[16] H.H. Kim, Y. Teramoto, N. Negishi, A. Ogata, Catal. Today 256 (2015) 13.

[17] C.C. Wu, C.I. Wu, J.C. Sturm, A. Kahn, Appl. Phys. Lett. 70 (1997) 1348.

[18] A.I. Pylinina, I.I. Mikhalenko, Theor. Exp. Chem. 49 (2013) 65.

[19] V. Demidyuk, J.C. Whitehead, Plasma Chem. Plasma Process. 27 (2007) 85.

[20] C.J. Liu, R. Mallison, L. Lobban, J. Catal. 179 (1998) 326.

[21] Y.F. Guo, D.Q. Ye, K.F. Chen, J.C. He, W.L. Chen, J. Mol. Catal. A 245 (2006) 93.

[22] E.C. Neyts, Plasma Chem. Plasma Process. 2015, DOI:10.1007/s11090-015-9662-5.

[23] W.S. Kang, J.M. Park, Y. Kim, S.H. Hong, IEEE Trans. Plasma Sci. 31 (2003) 504.

[24] J.S. Chang, K.G. Kostov, K. Urashima, T. Yamamoto, Y. Okayasu, T. Kato, T. Iwaizumi, K. Yoshimura, IEEE Trans. Ind. Appl. 36 (2000) 1251.

[25] T. Takuma, IEEE Trans. Electr. Insul. 26 (1991) 500.
[26] A. Ogata, D. Ito, K. Mizuno, S. Kushiyama, T. Yamamoto, IEEE Trans. Ind. Appl. 37 (2001) 959.
[27] A. Rousseau, O. Guaitella, J. Ropcke, L.V. Gatilova, Y.A. Tolmachev, Appl. Phys. Lett. 85 (2004) 2199.
[28] F. Holzer, U. Roland, F.D. Kopinke, Appl. Catal. B: Environ. 38 (2002) 163.
[29] U. Roland, F. Holzer, F.D. Kopinke, Appl. Catal. B: Environ. 58 (2005) 217.
[30] F. Holzer, F.D. Kopinke, U. Roland, Plasma Chem. Plasma Process. 25 (2005) 595.
[31] K. Hensel, S. Katsura, A. Mizuno, IEEE Trans. Plasma Sci. 33 (2005) 574.
[32] K. Hensel, V. Martisovits, Z. Machala, M. Janda, M. Lestinsky, P. Tardiveau, A. Mizuno, Plasma Process. Polym. 4 (2007) 682.
[33] K. Hensel, Eur. Phys. J. D 54 (2009) 141.
[34] M.B. Chang, J.H. Balbach, M.J. Rood, M.J. Kushner, J. Appl. Phys. 69 (1991) 4409.
[35] Ch. Subrahmanyam, M. Magureanu, A. Renken, L. Kiwi-Minsker, Appl. Catal. B: Environ. 65 (2006) 150.
[36] N.-L. Michels, S. Mitchell, M. Milina, K. Kunze, F. Krumeich, F. Marone, M. Erdmann, N. Marti, J. Perez-Ramirez, Adv. Funct. Mater. 22 (2012) 2509.
[37] J. Lefevere, M. Gysen, S. Mullens, V. Meynen, J. Van Noyen, Catal. Today 216 (2013)18.
[38] J. Lefevere, S. Mullens, V. Meynen, J. Van Noyen, Chemical Papers 68 (2014) 1143.
[39] J. Gascon, J.R. van Ommen, J.A. Moulijn, F. Kapteijn, Catal. Sci. Technol. 5 (2015) 807.
[40] Comsol Website; http://www.comsol.com
[41] U. Kogelschatz, Plasma Chem. Plasma Process. 23 (2003) 1.
[42] T. Yokoyama, M. Kogoma, T. Moriwaki, S. Okazaki, J. Phys. D: Appl. Phys. 23 (1990) 1125.
[43] K. Van Laer, A. Bogaerts, Energy Technol. 3 (2015) 1038.
[44] G.J.M. Hagelaar, L.C. Pitchford, Plasma Sources Sci. Technol. 14 (2005) 722.
[45] Morgan database, www.lxcat.net, retrieved on July 25, 2013.
[46] T. Martens, A. Bogaerts, W. Brok, J. van Dijk, Anal. Bioanal. Chem. 288 (2007) 1583.
[47] Q. Wang, D.J. Economou, V.M. Donnelly, J. Appl. Phys. 100 (2006) 023301.
[48] P.L. Patterson, Phys. Rev. A 2 (1970) 1154.
[49] A.N. Bhoj, M.J. Kushner, Plasma Sources Sci. Technol. 17 (2008) 035024.

Figure Captions

Fig. 1. Geometry used in the model (a), and magnification of the pore structure (b).

Fig. 2. Distributions of the electron density (a) and total ion density (b), averaged over one period, for a helium discharge sustained at 20 kV with a 100 μm pore. The same color scale is used for both densities, to allow comparison, but the values above and below the color scale indicate the maximum and minimum densities in each case.

Fig. 3. Distributions of the mean electron temperature (a) and electric field (b), averaged over one period, for a helium discharge sustained at 20 kV with a 100 μm pore.

Fig. 4. Distributions of the He^* density (a) and He_2^* density (b), averaged over one period, for a helium discharge sustained at 20 kV with a 100 μm pore.

Fig. 5. Distribution of the mean electron impact ionization rate, averaged over one period, for a helium discharge sustained at 20 kV with a 100 μm pore.

Fig. 6. Distribution of the electric potential in 2D (a), the potential along the horizontal direction at 7 different axial positions (cf. Fig. 1(b)) (b), and the potential along the vertical direction at the centerline (c), again averaged over one period, for a helium discharge sustained at 20 kV with a 100 μm pore.

Fig. 7. Distributions of the electron density (a) and total ion density (b) along the vertical centerline for different pore sizes, for a helium discharge sustained at 20 kV.

Fig. 8. Distributions of the electron temperature (a), electric field (b) and electron impact ionization rate (c) along the vertical centerline for different pore sizes, for a helium discharge sustained at 20 kV.

Fig. 9. Distributions of the potential for different pore sizes: (a) 10 μm, (b) 50 μm, (c) 400 μm, for a helium discharge sustained at 20 kV.

Fig. 10. Distributions of the electron density (a) and total ion density (b) along the vertical centerline for different applied voltages, for a helium discharge with a 30 μm pore.

Fig. 11. Distributions of the electron temperature (a), electric field (b) and electron impact ionization rate (c) along the vertical centerline for different applied voltages, for a helium discharge with a 30 μm pore.

Fig. 12. Distributions of the potential for different applied voltages: (a) 2 kV, (b) 20 kV, (c) 100 kV, for a helium discharge with a 30 μm pore.

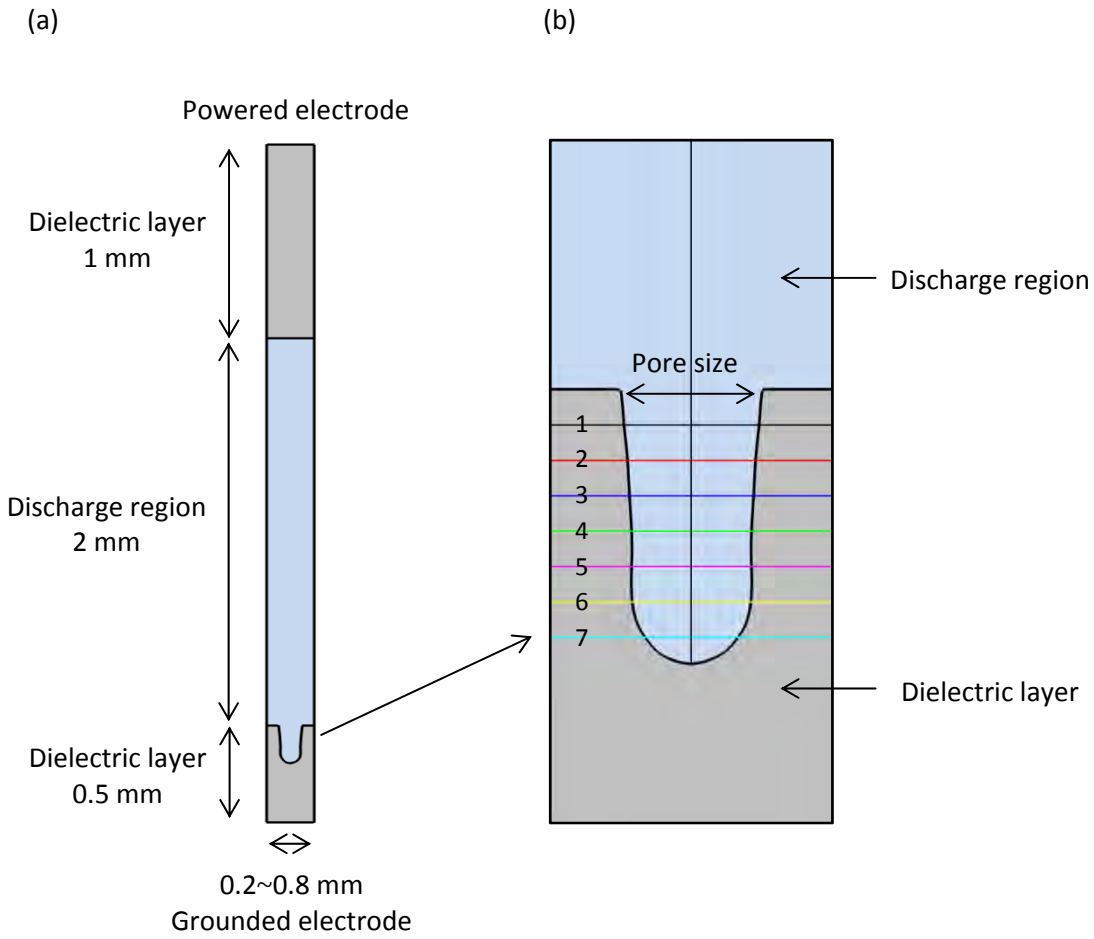
(a)
(b)
Powered electrode
Dielectric layer
1 mm
Discharge region
2 mm
Dielectric layer
0.5 mm
0.2~0.8 mm
Grounded electrode
Discharge region
Pore size
1
2
3
4
5
6
7
Dielectric layer

Figure 1

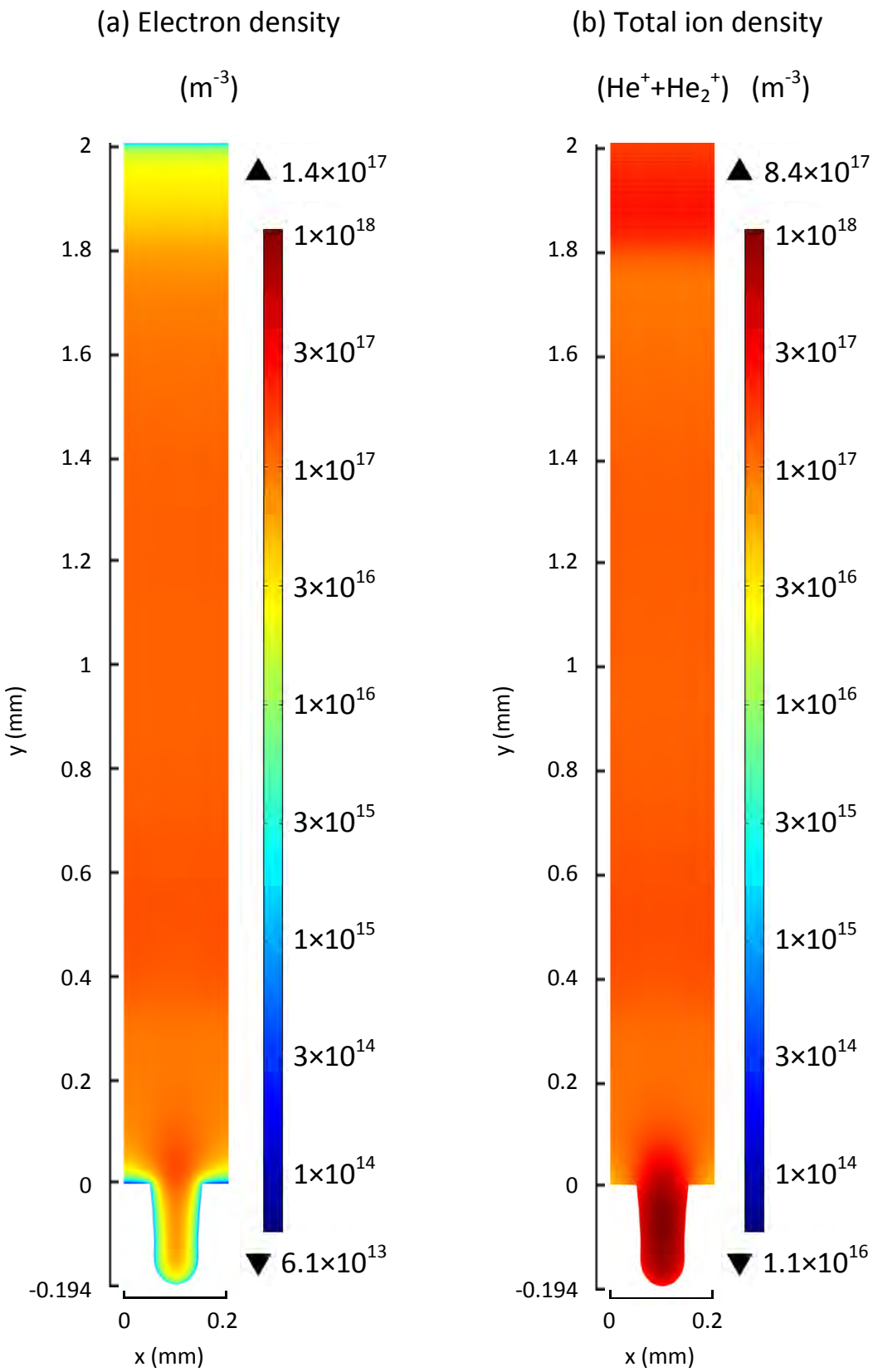
(a) Electron density
(m-3)
(b) Total ion density
(He+ +He2+) (m-3)
y (mm)
x (mm)
2
1.8
1.6
1.4
1.2
1
0.8
0.6
0.4
0.2
0
-0.194
0
0.2
▲ 1.4×10^17
1×10^18
3×10^17
1×10^17
3×10^16
1×10^16
3×10^15
1×10^15
3×10^14
1×10^14
▼ 6.1×10^13
▲ 8.4×10^17
1×10^18
3×10^17
1×10^17
3×10^16
1×10^16
3×10^15
1×10^15
3×10^14
1×10^14
▼ 1.1×10^16

Figure 2

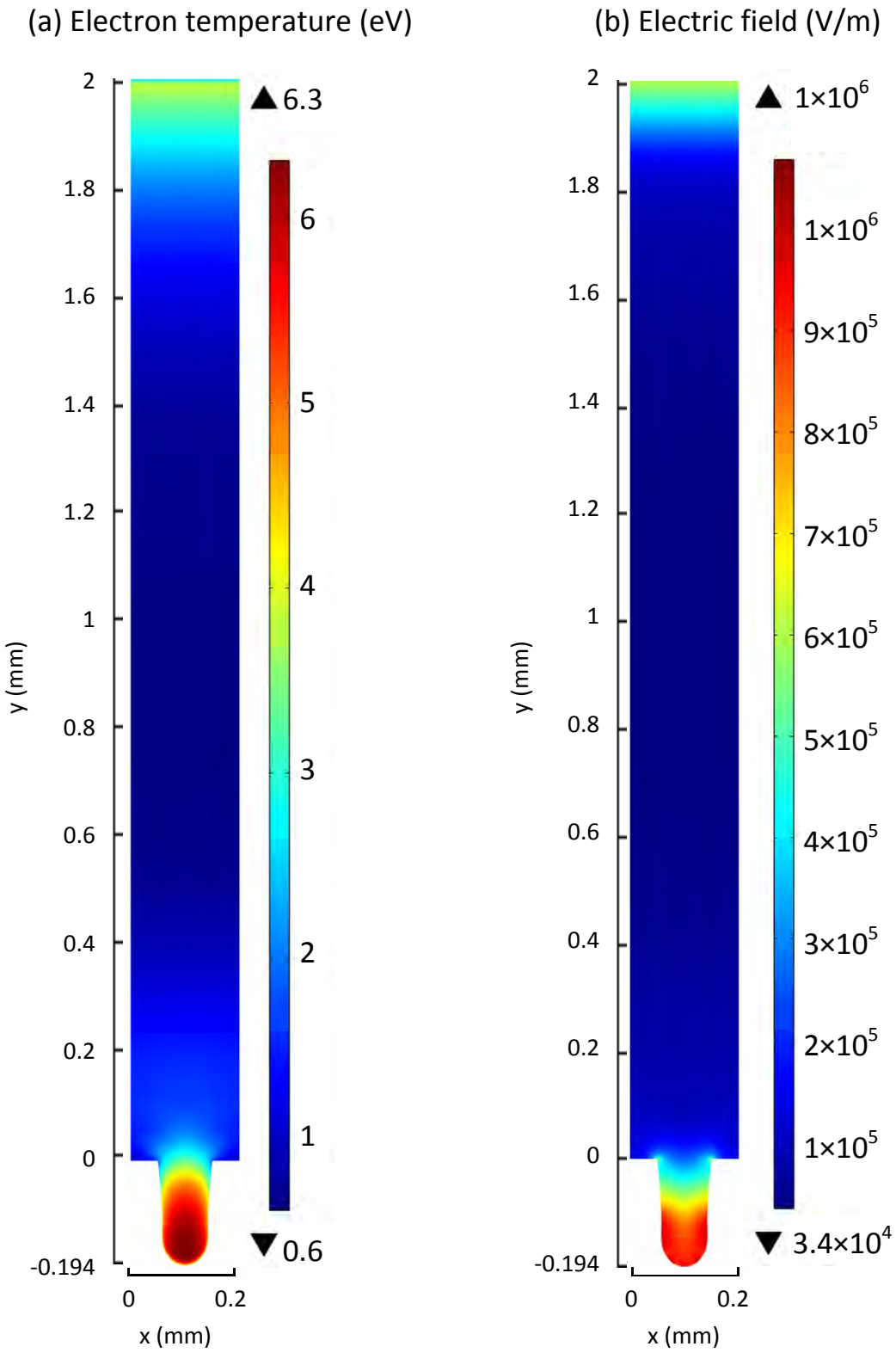
(a) Electron temperature (eV)
(b) Electric field (V/m)
y (mm)
x (mm)
2
1.8
1.6
1.4
1.2
1
0.8
0.6
0.4
0.2
0
-0.194
0
0.2
▲6.3
6
5
4
3
2
1
▼0.6
▲1×10^6
1×10^6
9×10^5
8×10^5
7×10^5
6×10^5
5×10^5
4×10^5
3×10^5
2×10^5
1×10^5
▼3.4×10^4

Figure 3

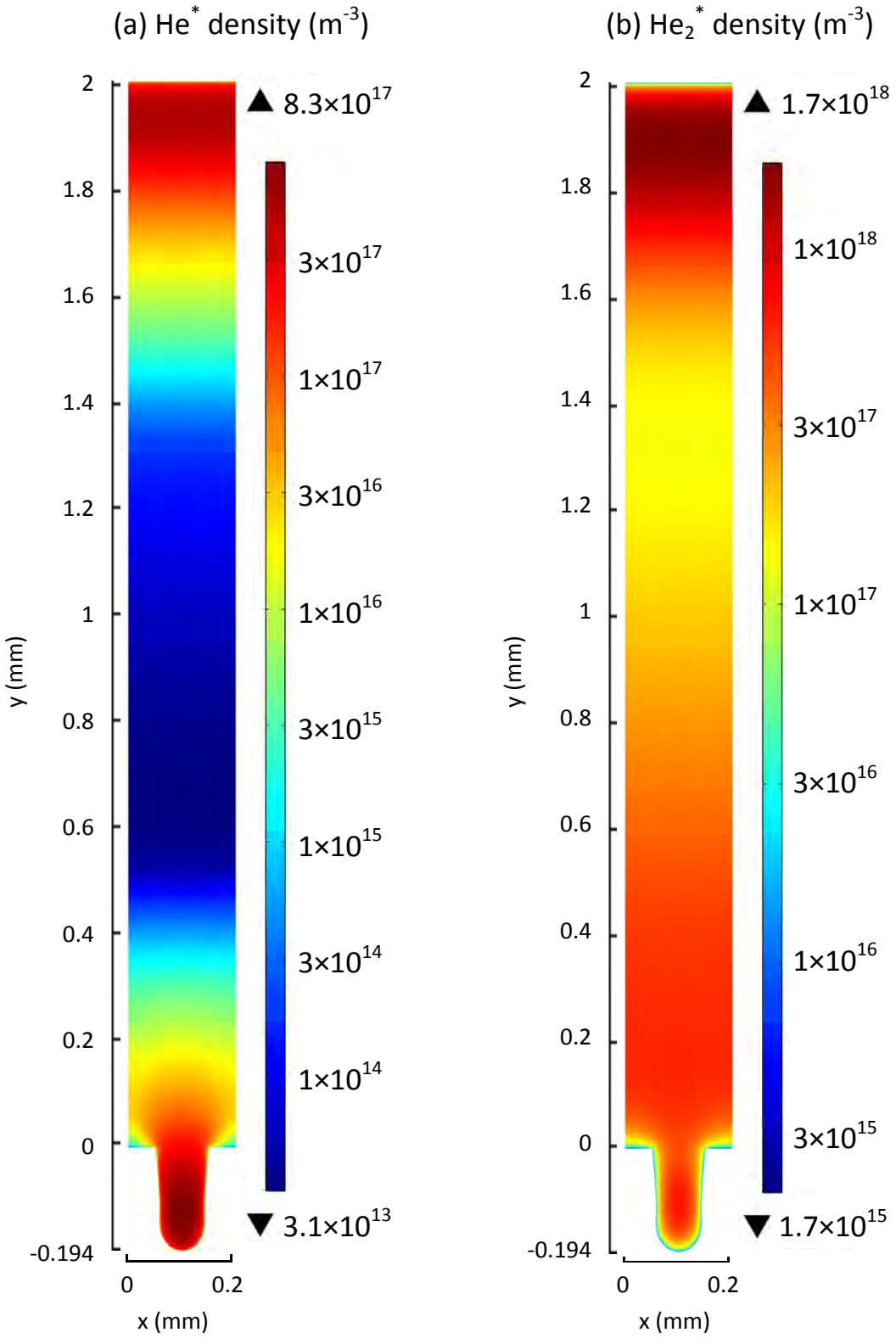
(a) He* density (m-3)
(b) He2* density (m-3)
y (mm)
x (mm)
2
1.8
1.6
1.4
1.2
1
0.8
0.6
0.4
0.2
0
-0.194
0
0.2
▲ 8.3×10^17
3×10^17
1×10^17
3×10^16
1×10^16
3×10^15
1×10^15
3×10^14
1×10^14
▼ 3.1×10^13
▲ 1.7×10^18
1×10^18
3×10^17
1×10^17
3×10^16
1×10^16
3×10^15
▼ 1.7×10^15

Figure 4

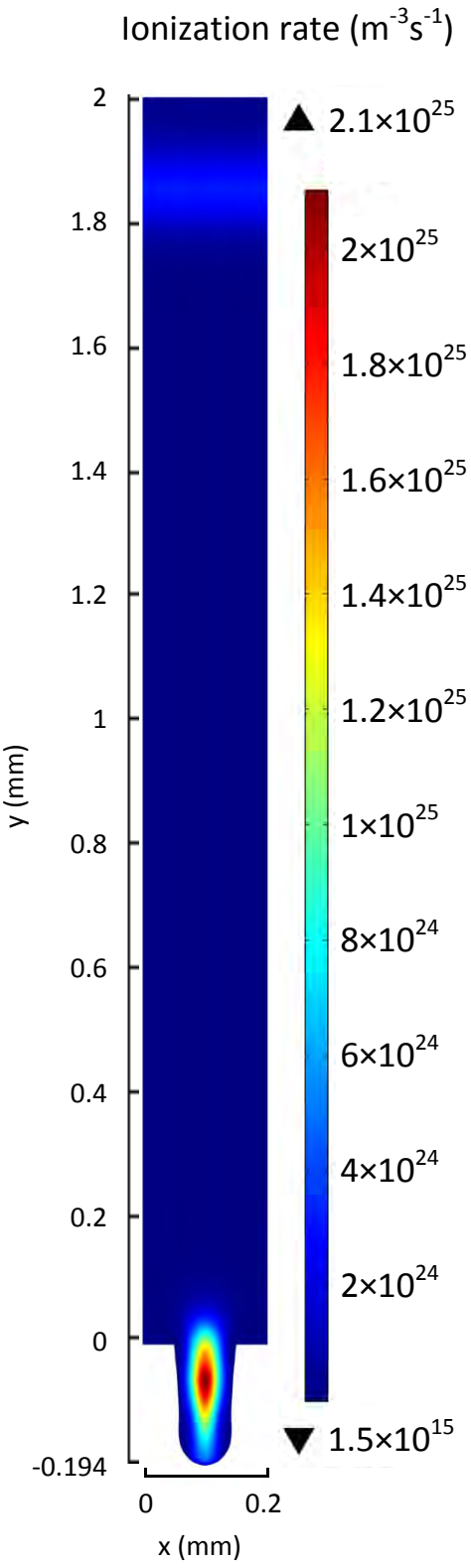
Ionization rate ($m^{-3}s^{-1}$)
2.1×10^{25}
2×10^{25}
1.8×10^{25}
1.6×10^{25}
1.4×10^{25}
1.2×10^{25}
1×10^{25}
8×10^{24}
6×10^{24}
4×10^{24}
2×10^{24}
1.5×10^{15}
y (mm)
2
1.8
1.6
1.4
1.2
1
0.8
0.6
0.4
0.2
0
-0.194
0
0.2
x (mm)

Figure 5

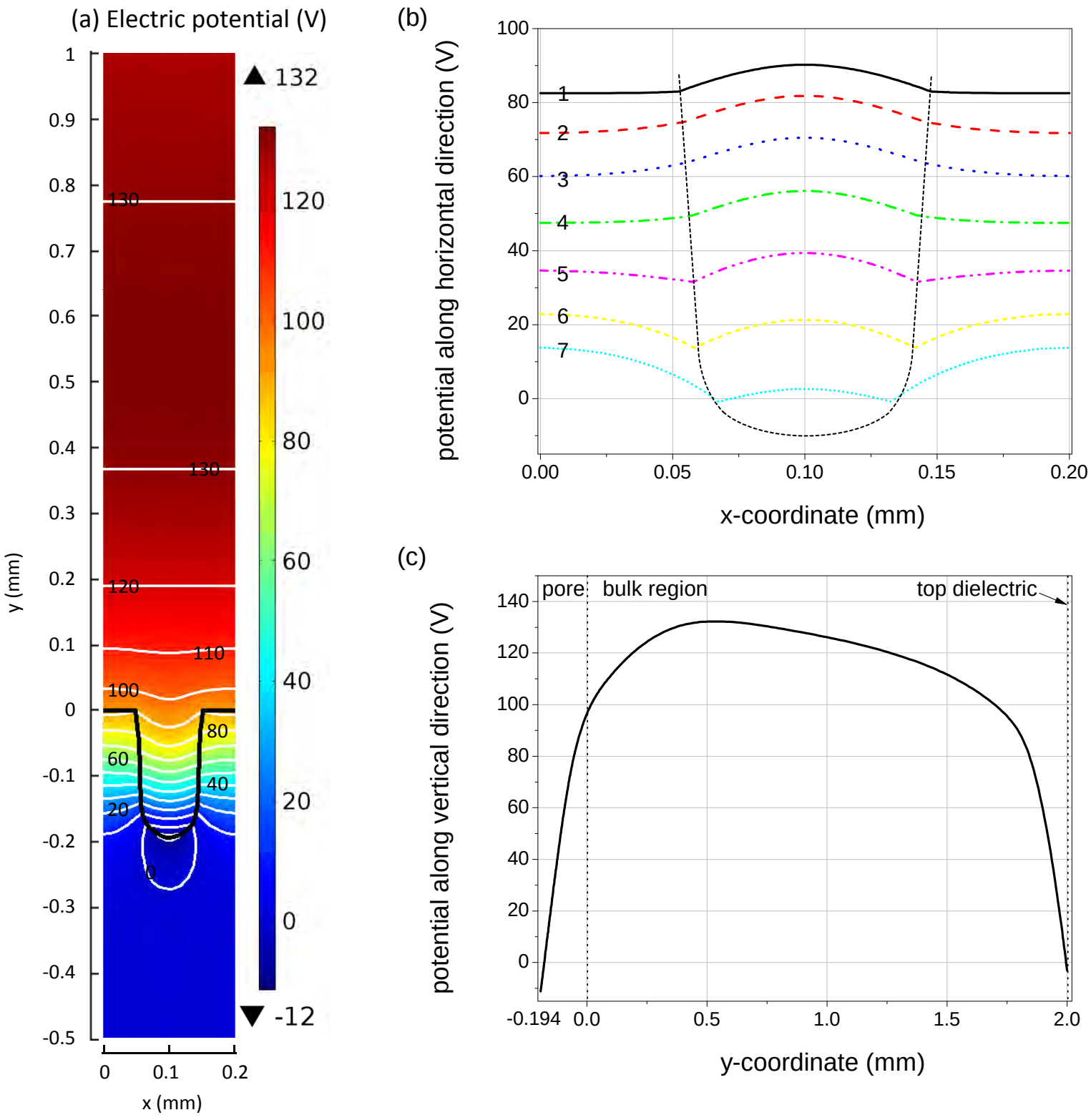
(a) Electric potential (V)
▲ 132
120
100
80
60
40
20
0
▼ -12
130
130
120
110
100
80
60
40
20
0
y (mm)
x (mm)
(b)
potential along horizontal direction (V)
x-coordinate (mm)
1
2
3
4
5
6
7
(c)
potential along vertical direction (V)
y-coordinate (mm)
pore
bulk region
top dielectric

Figure 6

(a)

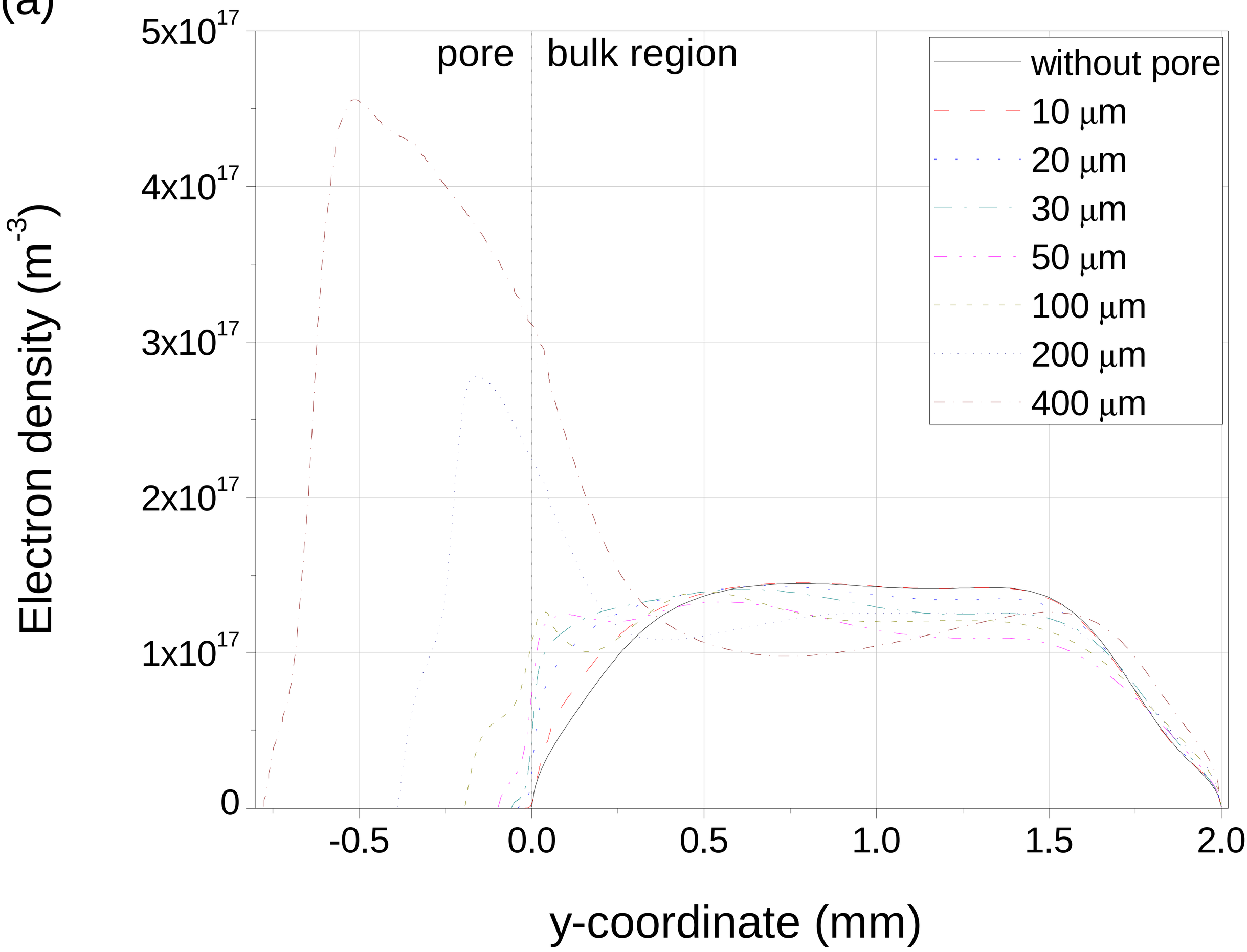
pore
bulk region
without pore
10 μm
20 μm
30 μm
50 μm
100 μm
200 μm
400 μm
Electron density (m-3)
5x10^17
4x10^17
3x10^17
2x10^17
1x10^17
0
-0.5
0.0
0.5
1.0
1.5
2.0
y-coordinate (mm)

(b)

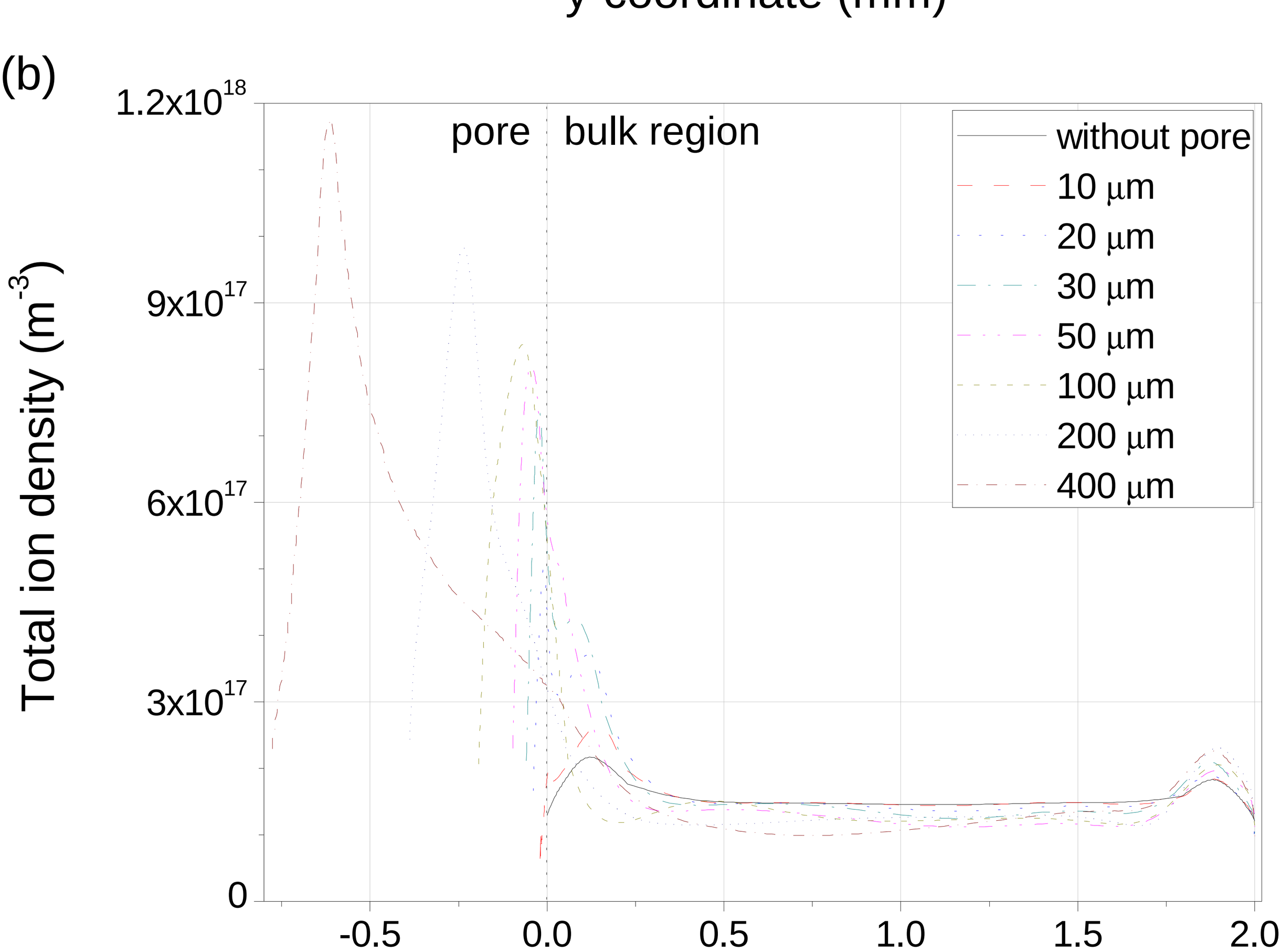
pore
bulk region
without pore
10 μm
20 μm
30 μm
50 μm
100 μm
200 μm
400 μm
Total ion density (m-3)
1.2x10^18
9x10^17
6x10^17
3x10^17
0
-0.5
0.0
0.5
1.0
1.5
2.0
y-coordinate (mm)

Figure 7

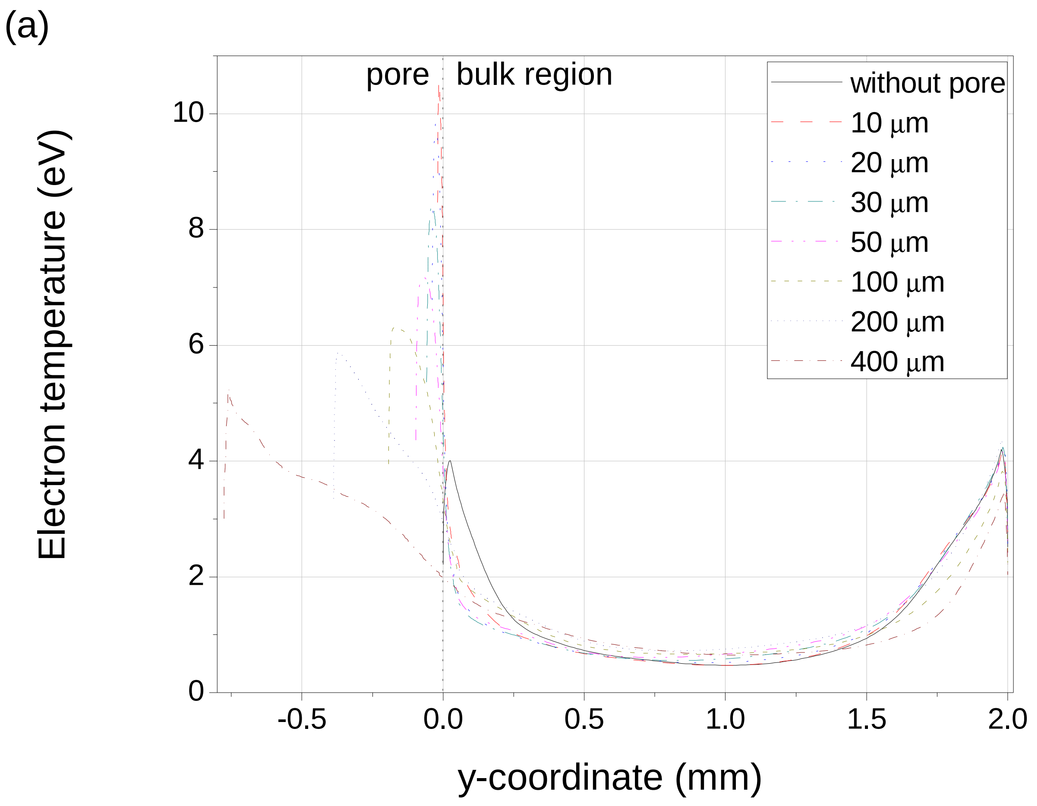
(a)
pore
bulk region
without pore
10 μm
20 μm
30 μm
50 μm
100 μm
200 μm
400 μm
Electron temperature (eV)
0
2
4
6
8
10
-0.5
0.0
0.5
1.0
1.5
2.0
y-coordinate (mm)

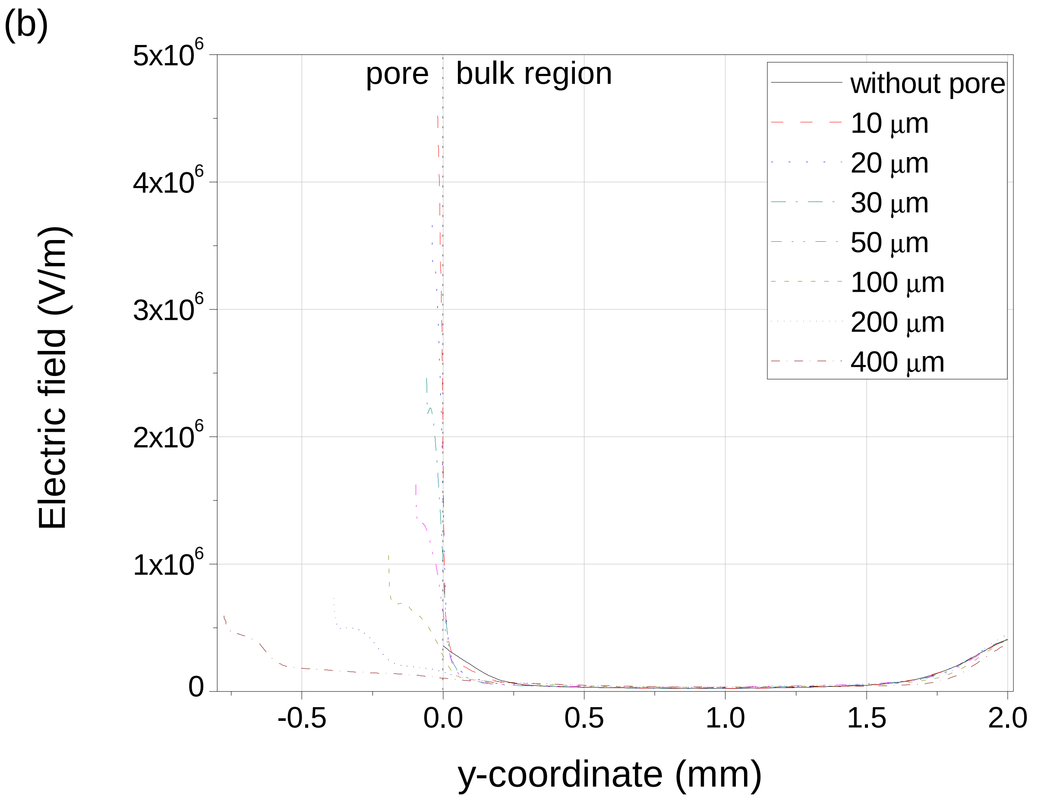
(b)
pore
bulk region
without pore
10 μm
20 μm
30 μm
50 μm
100 μm
200 μm
400 μm
Electric field (V/m)
0
1x10^6
2x10^6
3x10^6
4x10^6
5x10^6
-0.5
0.0
0.5
1.0
1.5
2.0
y-coordinate (mm)

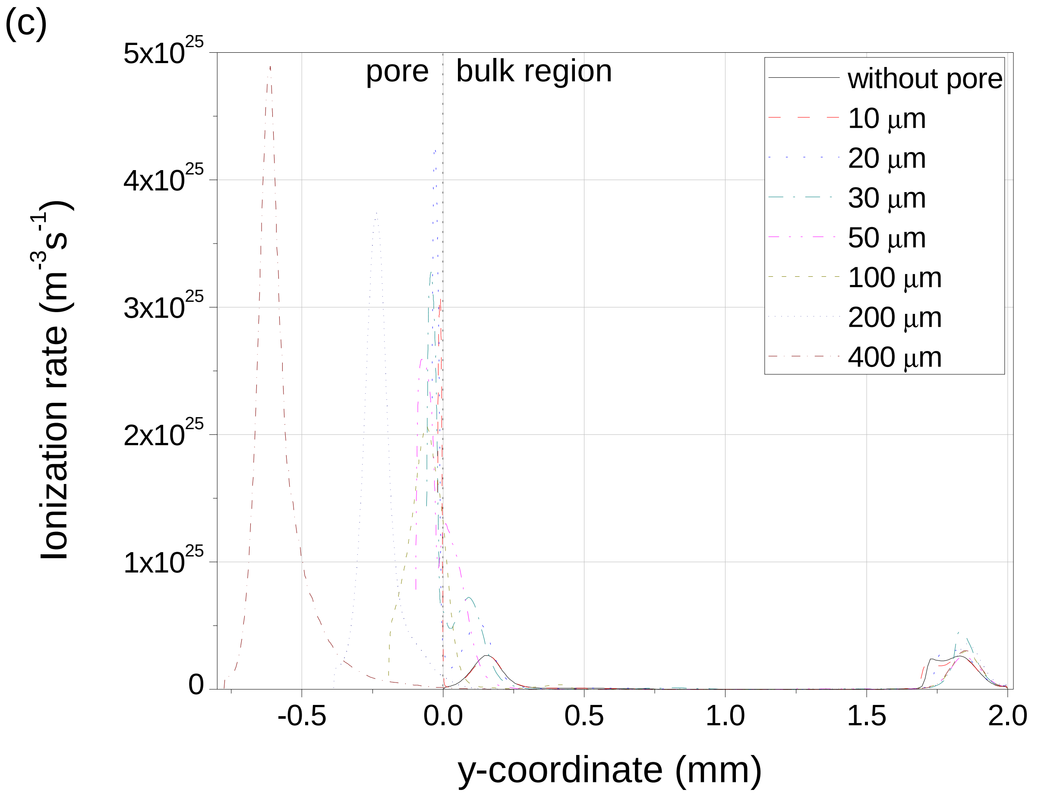
(c)
pore
bulk region
without pore
10 μm
20 μm
30 μm
50 μm
100 μm
200 μm
400 μm
Ionization rate (m^-3 s^-1)
0
1x10^25
2x10^25
3x10^25
4x10^25
5x10^25
-0.5
0.0
0.5
1.0
1.5
2.0
y-coordinate (mm)

Figure 8

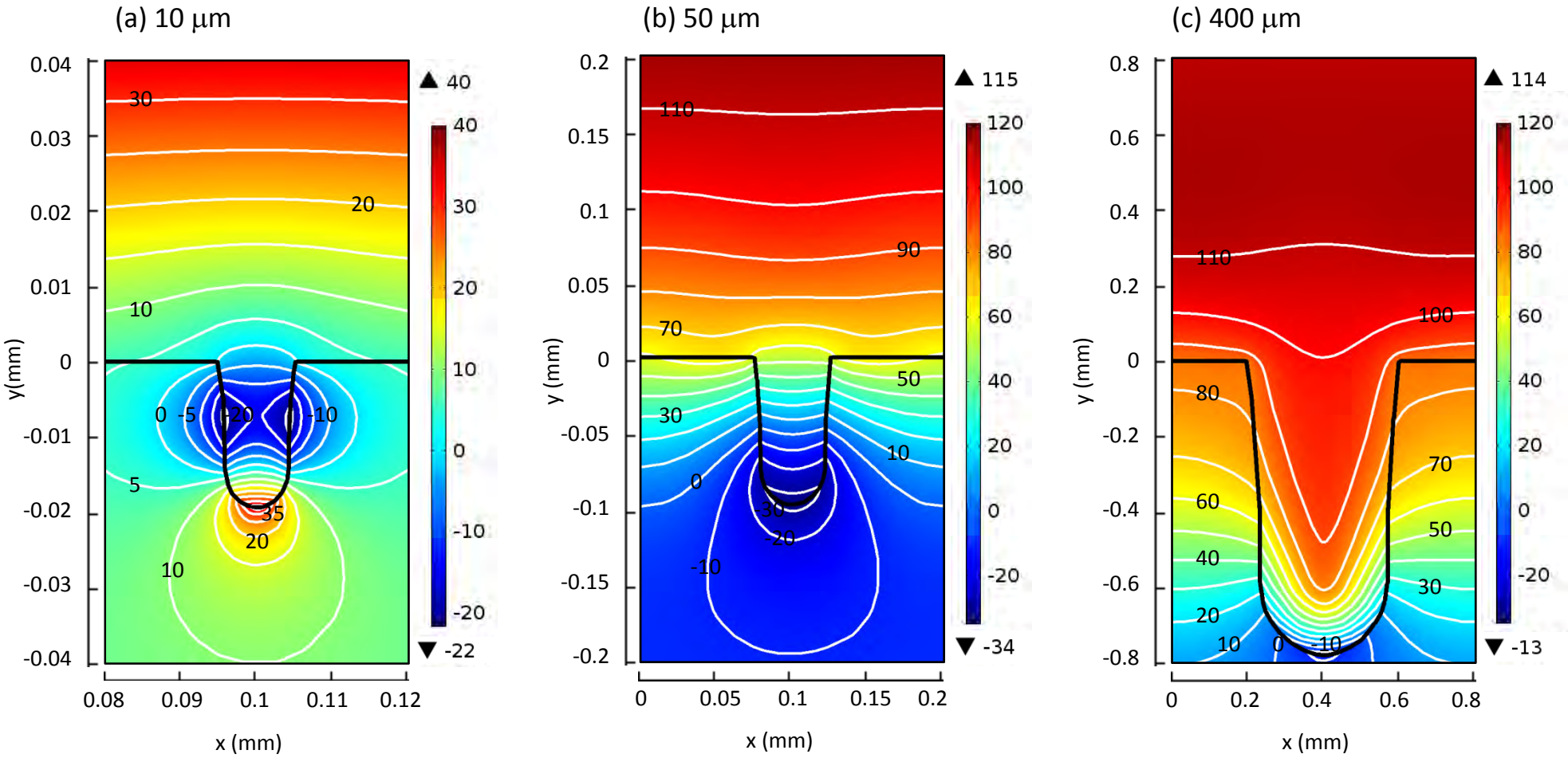

Figure 9

(a)

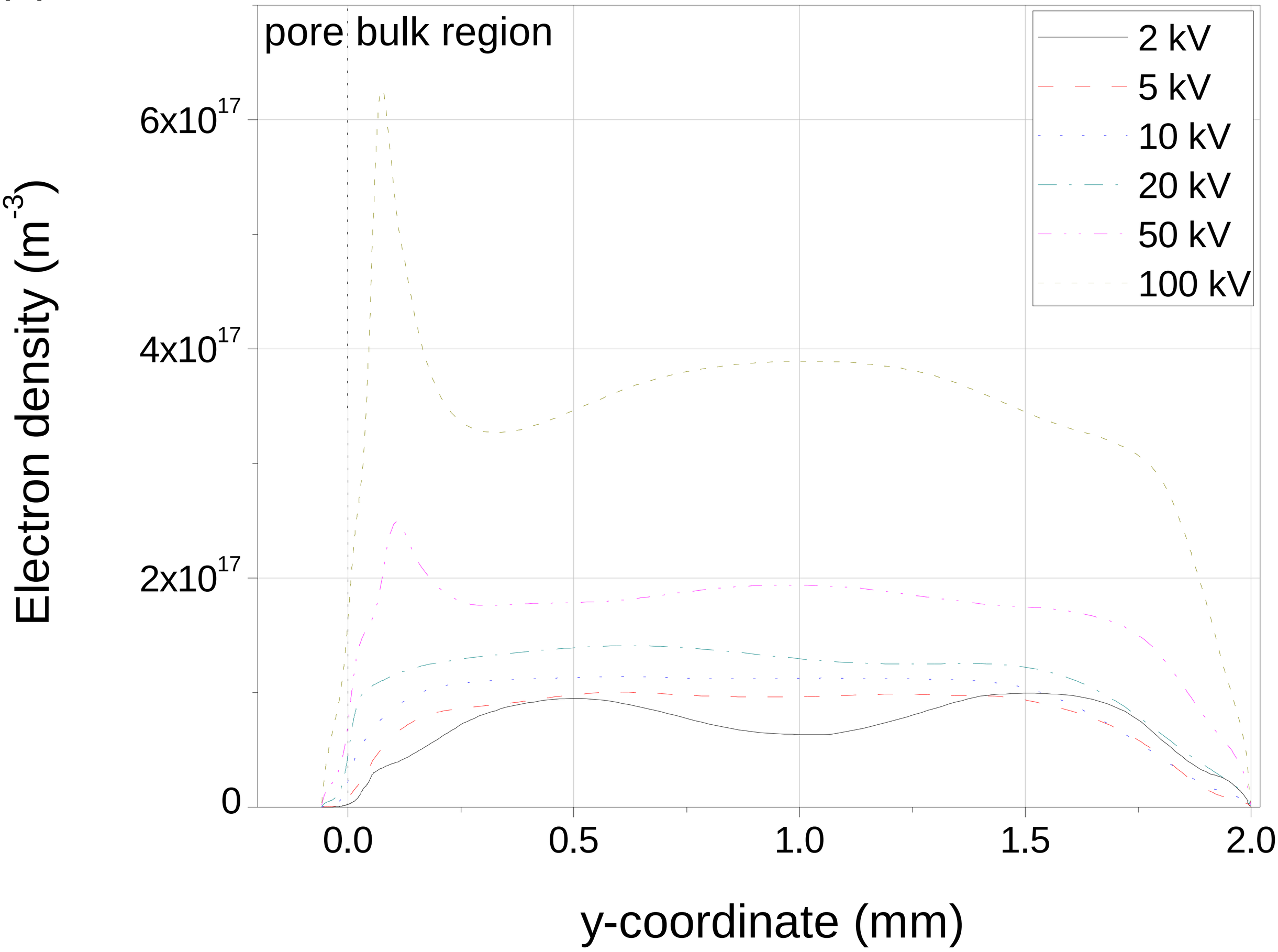
pore
bulk region
2 kV
5 kV
10 kV
20 kV
50 kV
100 kV
Electron density (m-3)
6x1017
4x1017
2x1017
0
0.0
0.5
1.0
1.5
2.0
y-coordinate (mm)

(b)

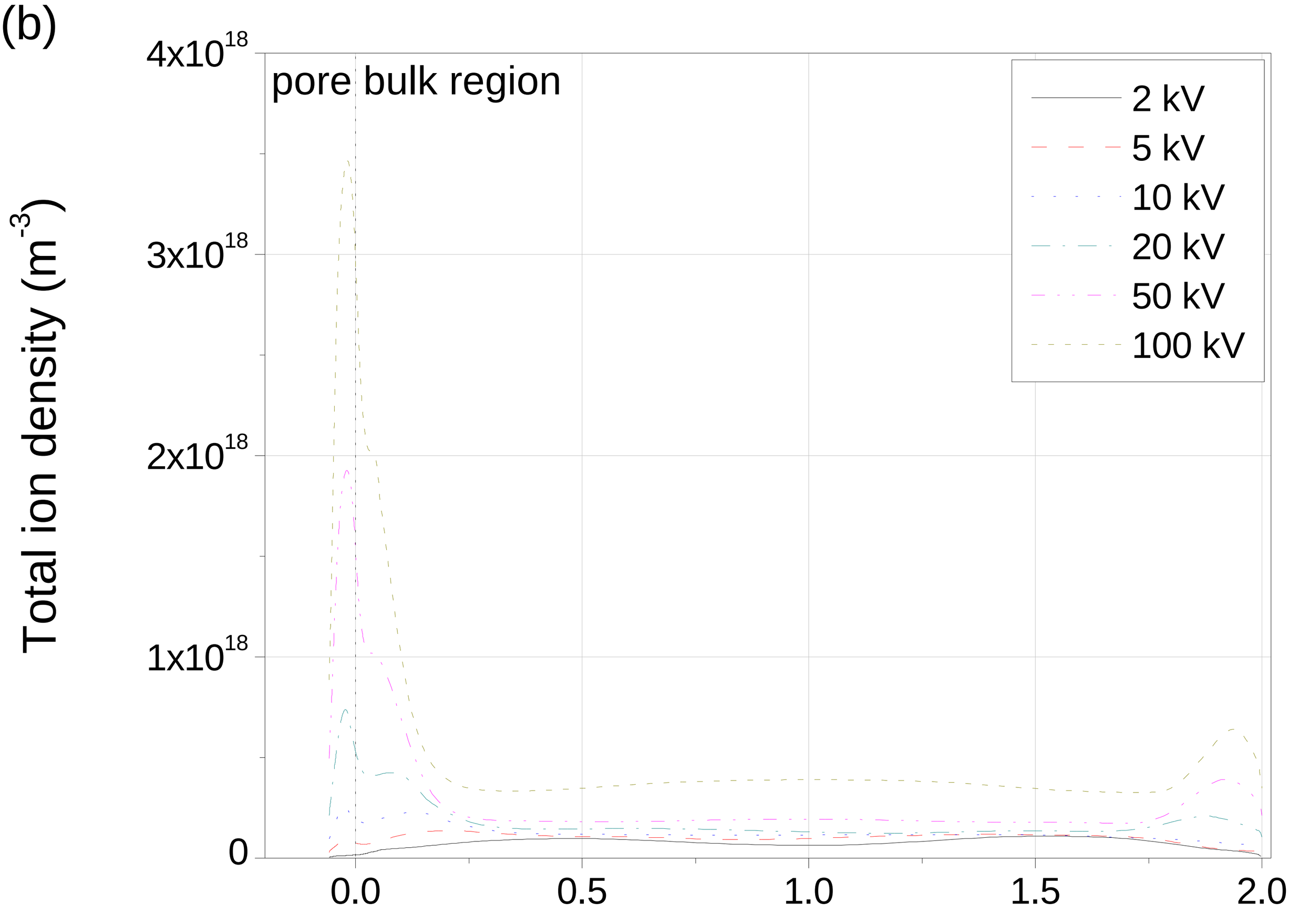
pore
bulk region
2 kV
5 kV
10 kV
20 kV
50 kV
100 kV
Total ion density (m-3)
4x1018
3x1018
2x1018
1x1018
0
0.0
0.5
1.0
1.5
2.0
y-coordinate (mm)

Figure 10

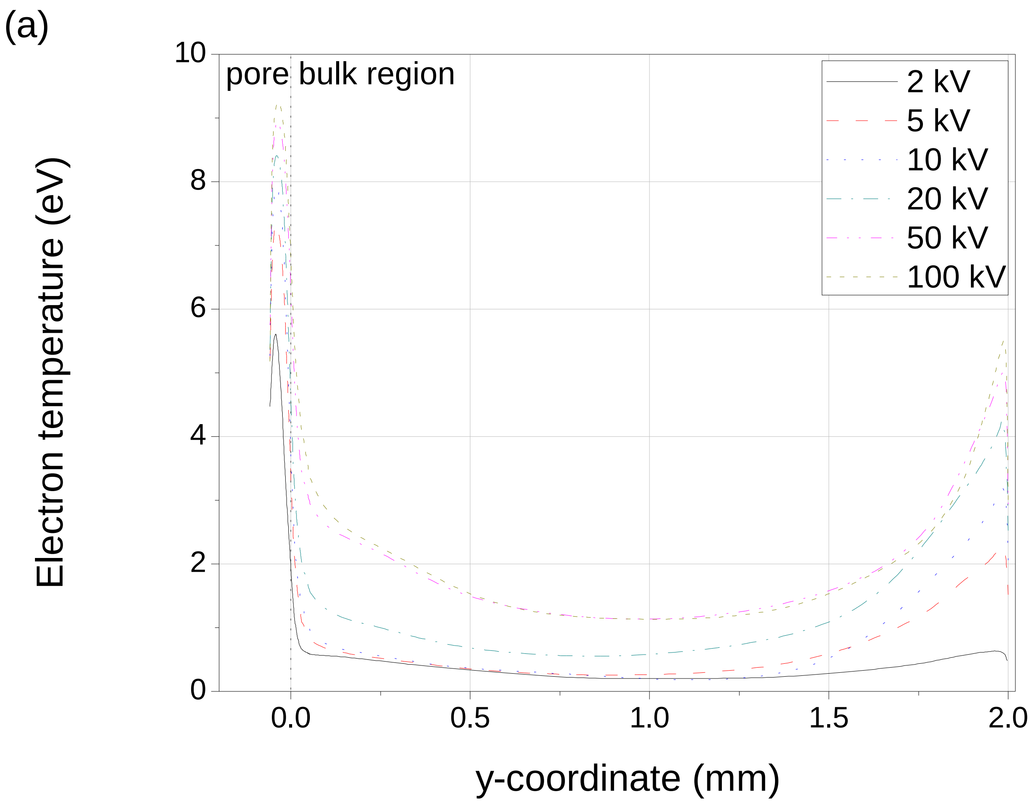
(a)
pore bulk region
2 kV
5 kV
10 kV
20 kV
50 kV
100 kV
Electron temperature (eV)
0
2
4
6
8
10
0.0
0.5
1.0
1.5
2.0
y-coordinate (mm)

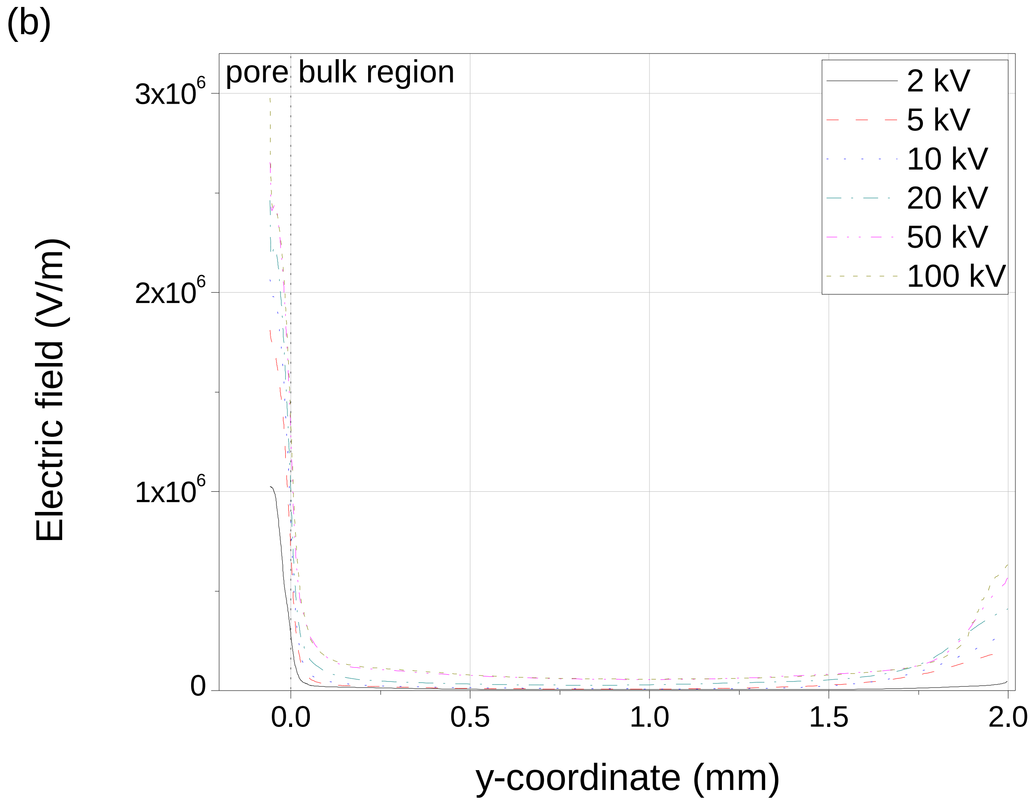
(b)
pore bulk region
2 kV
5 kV
10 kV
20 kV
50 kV
100 kV
Electric field (V/m)
0
1x10^6
2x10^6
3x10^6
0.0
0.5
1.0
1.5
2.0
y-coordinate (mm)

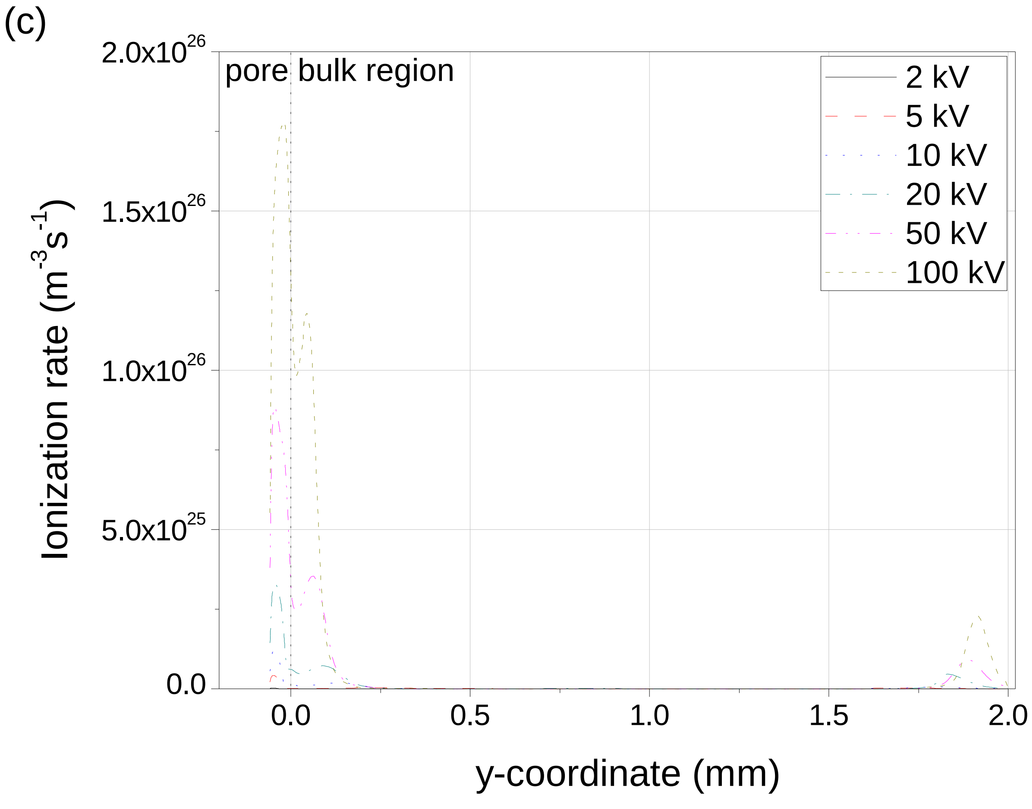
(c)
pore bulk region
2 kV
5 kV
10 kV
20 kV
50 kV
100 kV
Ionization rate (m^-3 s^-1)
0.0
5.0x10^25
1.0x10^26
1.5x10^26
2.0x10^26
0.0
0.5
1.0
1.5
2.0
y-coordinate (mm)

Figure 11

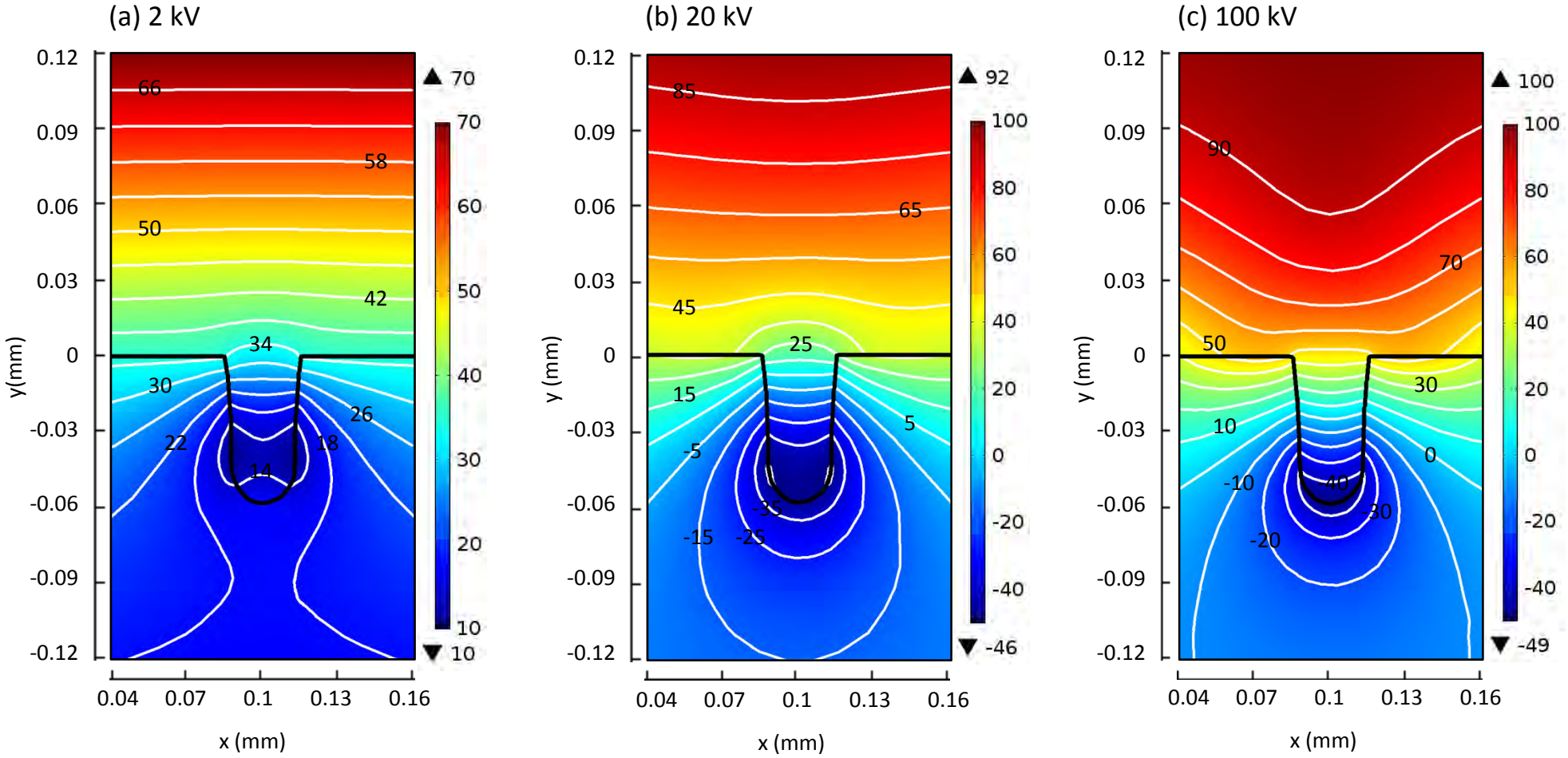
(a) 2 kV
(b) 20 kV
(c) 100 kV
y(mm)
y (mm)
x (mm)
0.12
0.09
0.06
0.03
0
-0.03
-0.06
-0.09
-0.12
0.04
0.07
0.1
0.13
0.16
66
58
50
42
34
30
26
22
18
14
▲ 70
▼ 10
85
65
45
25
15
5
-5
-15
-25
-35
▲ 92
▼ -46
90
70
50
30
10
0
-10
-20
-30
-40
▲ 100
▼ -49

Figure 12